

Spatiotemporal Evolution of Slow Slip Events at the Offshore Hikurangi Subduction Zone in 2019 using GNSS, InSAR, and seafloor geodetic data

K. Woods¹, L. M. Wallace^{2,3,4}, C. A. Williams⁵, I. J. Hamling⁵, S. C. Webb⁶, Y. Ito⁷, N. Palmer⁵, R. Hino⁸, S. Suzuki⁸, M. K. Savage¹, E. Warren-Smith⁵ and K. Mochizuki⁹

¹School of Geography, Environment and Earth Sciences, Victoria University of Wellington, Wellington, New Zealand.

² GEOMAR Helmholtz Centre for Ocean Research, Kiel, Germany.

³ Institute of Geosciences, Christian-Albrechts-Universität zu Kiel, Kiel, Germany

⁴Institute for Geophysics, University of Texas, Austin, Texas, USA.

⁵GNS Science, Lower Hutt, New Zealand

⁶Lamont-Doherty Earth Observatory, Columbia University, Palisades, New York, USA.

⁷Disaster Prevention Research Institute, Kyoto University, Kyoto, Japan.

⁸Graduate School of Science, Tohoku University, Sendai, Japan.

⁹Earthquake Research Institute, University of Tokyo

Corresponding author: Laura Wallace (lwallace@utexas.edu)

Key Points:

- Central Hikurangi slow slip events propagate up-dip over a period of weeks to months
 - Seafloor geodetic data reveal that shallow slow slip events may last longer than onshore GNSS data suggest
 - The same portions of a shallow megathrust can host both large seismic and aseismic rupture

23 Abstract

24 Detecting crustal deformation during transient deformation events at offshore subduction zones
25 remains challenging. The spatiotemporal evolution of slow slip events (SSEs) on the offshore
26 Hikurangi subduction zone, New Zealand, during February–July 2019, is revealed through a
27 time-dependent inversion of onshore and offshore geodetic data that also account for spatially
28 varying elastic crustal properties. Our model is constrained by seafloor pressure time series (as a
29 proxy for vertical seafloor deformation), onshore continuous Global Navigation Satellite System
30 (GNSS) data, and Interferometric Synthetic Aperture Radar (InSAR) displacements. Large
31 GNSS displacements onshore and uplift of the seafloor (10–33 mm) require peak slip during the
32 event of 150 to >200 mm at 6–12 km depth offshore Hawkes Bay and Gisborne, comparable to
33 maximum slip observed during previous seafloor pressure deployments at north Hikurangi. The
34 onshore and offshore data reveal a complex evolution of the SSE, over a period of months.
35 Seafloor pressure data indicates the slow slip may have persisted longer near the trench than
36 suggested by onshore GNSS stations in both the Gisborne and Hawkes Bay regions. Seafloor
37 pressure data also reveal up-dip migration of SSE slip beneath Hawke Bay occurred over a
38 period of a few weeks. The SSE source region appears to coincide with locations of the March
39 1947 M_w 7.0–7.1 tsunami earthquake offshore Gisborne and estimated Great earthquake rupture
40 sources from paleoseismic investigations offshore Hawkes Bay, suggesting that the shallow
41 megathrust at north and central Hikurangi is capable of both seismic and aseismic rupture.

42

43 Plain Language Summary

44 Subduction zones, where one tectonic plate dives beneath another are where the planet's largest
45 earthquakes are generated. They also host an important mode of fault slip called “slow slip
46 events”, which are essentially earthquakes in slow motion. The Hikurangi subduction zone,
47 where the Pacific Plate subducts beneath New Zealand hosts large and frequent slow slip events
48 near the trench, where the plate boundary emerges at the seabed, requiring seafloor
49 instrumentation to investigate them. Seafloor pressure measurements can track centimeter-level
50 up or down movement of the seafloor during slow slip, and reveal offshore displacement during
51 a large 2019 slow slip event at the offshore Hikurangi subduction zone. The 2019 event involved
52 substantial migration from ~15 km depth to the trench over a period of several weeks. We also

53 show that the same areas which have ruptured in previous seismic earthquakes (that involved
54 faster slip) can also rupture slowly, in slow slip events. This raises the possibility that regions
55 that we currently observe to produce slow slip events could also produce seismic events. This
56 result also demands that more work must be done to understand the physical processes that
57 enable the same part of a fault to rupture both fast and slow.

58 **1 Introduction**

59 Continuous Global Navigation Satellite System (GNSS) stations are typically used to
60 monitor slow slip events (SSEs) located near or beneath onshore networks. For many subduction
61 zones, this is typically restricted to the deeper portions of megathrusts (>30 km depth) that
62 underlie land. This creates a major blind-spot for transient deformation events occurring on
63 offshore subduction zones, which are not amenable to detection and detailed characterization
64 with conventional land-based monitoring techniques. This greatly limits our ability to resolve
65 how tectonic strain is accumulated and released near the trench at subduction zones, in regions
66 where the world's largest and deadliest tsunamis are also generated. Several techniques have
67 been developed over the last 10-20 years to fill this major observational gap, including GNSS-
68 Acoustic arrays (for horizontal displacement rates relative to a known, terrestrial reference
69 frame), Absolute Pressure Gauges (APGs; to detect transient vertical deformation), Direct-path
70 Acoustic Ranging (for horizontal deformation over short distances), and offshore borehole
71 observations of pore pressure changes (as a proxy for volumetric strain) (Gagnon et al., 2005;
72 Bürgmann and Chadwell, 2014; Davis et al., 2015; Wallace et al., 2016; Araki et al., 2017;
73 Urlaub et al., 2018; Yokota and Ishikawa, 2020). Without such instrumentation, understanding of
74 shallow, near-trench slow slip and interseismic coupling, and the processes that produce these
75 behaviors is limited.

76 At the Hikurangi subduction zone offshore New Zealand, the Pacific plate subducts
77 westward beneath the North Island at rates of 20–60 mm/yr (Wallace et al., 2004). The
78 subduction plate boundary is located at 12-15 km depth beneath the east coast of the North Island
79 (Williams et al., 2013) and the trench is located 80-100 km offshore, providing a situation where
80 both shallow (~10-15 km) and deep (>25 km) SSEs can be observed using the land-based
81 continuous GNSS (cGNSS) network operated by GeoNet (www.geonet.org.nz) (see Wallace,
82 2020, and references therein).

83 Frequent, shallow SSEs (<15 km) occur primarily offshore at the northern and central
84 Hikurangi margin, recurring every 1–2 years, and lasting from one week to several months
85 (Wallace and Beavan, 2010; Wallace et al., 2012b, 2013, 2016; Koulali et al., 2017). The largest
86 shallow Hikurangi SSEs (in 2004, 2010, 2014, and 2019) have produced up to 40 mm of
87 horizontal surface displacements at coastal cGNSS stations. Most shallow Hikurangi SSEs occur
88 on the portion of the plate boundary that appears to be mostly creeping over multiple SSE cycles
89 (based on models of interseismic coupling), while the deep SSEs occur at the down-dip transition
90 from deep locking to aseismic creep (Wallace et al., 2012a; Wallace, 2020). Although the
91 onshore cGNSS network is capable of detecting offshore SSEs, they are located too far from the
92 SSE source to provide detailed constraints on the spatio-temporal evolution of these events, and
93 in particular, whether or not they rupture to the trench. To address this, the 2014 Hikurangi
94 Ocean Bottom Investigation of Tremor and Slow Slip (HOBITSS) experiment was undertaken
95 offshore the Gisborne region to detect seafloor pressure changes during a large SSE in
96 September – October 2014. Using the seafloor pressure data from the array, Wallace et al. (2016)
97 demonstrated the ability of such a network to detect centimetre-level vertical displacement of the
98 seafloor during slow slip, and showed that the 2014 SSE may have reached the trench, with
99 implications for the range of physical conditions that can host slow slip.

100 Since the 2014/2015 HOBITSS Experiment, we have undertaken rolling deployments of
101 APGs and Ocean Bottom Seismometers (OBS) at the offshore Hikurangi margin to develop a
102 longer-term understanding of shallow SSE behavior and related seismicity there. A deployment
103 in 2018/2019 offshore Gisborne and Hawkes Bay (Barker et al., 2019) captured vertical seafloor
104 displacement during a large SSE in April-June 2019 (Woods et al., 2022). The 2019 SSE is the
105 largest SSE to occur since the large 2014 SSE captured by the HOBITSS experiment. The
106 deployment also represents the first time that APGs have been deployed offshore the central
107 Hikurangi margin, where the trench is furthest (~150 km) from land, and where offshore SSEs
108 are the most difficult to resolve with land-based data. To reveal the spatiotemporal evolution of
109 the 2019 SSE, we utilize the seafloor pressure timeseries (as a proxy for vertical deformation)
110 acquired during the 2018/2019 experiment, as well as three-component continuous GNSS time
111 series, and InSAR Line-of-Sight (LOS) displacements. This represents the first study to globally
112 undertake a joint inversion of GNSS, InSAR, and seafloor geodetic measurements. The
113 improved resolution of the offshore regions of the subduction zone provided by the APGs,

114 reveals new information about slip behaviour on the shallowest portions of subduction zone (not
115 detectable by the onshore GNSS network) including up-dip migration (towards the trench) of
116 slow slip beneath Hawke Bay.

117 **2 Geodetic observations of shallow Hikurangi subduction SSEs in 2019**

118 New Zealand's onshore continuous GNSS network (operated by GeoNet;
119 www.geonet.org.nz) detected a sequence of SSEs offshore the east coast of North Island between
120 February and July 2019 (Woods et al., 2022), with SSE phases of varying onset times and
121 durations along the margin (Figure 1). A small SSE was first detected just to the south of our
122 study area, south of Hawke Bay, with <5 mm eastward motion over 2–3 days in the first week of
123 March 2019 (see Pawanui (PAWA) GNSS station time series and green shading in Figure 1a).
124 Approximately three weeks later, beginning in late March, SSE signals were detected at the
125 Gisborne region, with up to 40 mm of eastward motion occurring over 4–5 weeks. The Gisborne
126 SSE displayed a particularly rapid phase of slip for the first week of the motion, as shown by the
127 Makorori (MAKO) GNSS time series (Figure 1a).

128 Longer duration SSE-related motion, involving <20 mm eastward displacement, was
129 observed further south at cGNSS sites in the Hawkes Bay area from early April until mid June
130 (see Cape Kidnappers (CKID) station and lavender shading in Figure 1a). Between the Gisborne
131 and Hawkes Bay regions, the GNSS station at Māhia Peninsula (MAHI) detected two rapid SSE
132 phases. 10 mm of eastward motion occurred in the first week of April, followed by more gradual
133 15–20 mm displacement (likely due to the ongoing SSEs near the Gisborne and Hawkes Bay
134 areas). A further ~10 mm of eastward motion occurred during the first two weeks of May (see
135 the light blue shading in the Figure 1a).

136 The onshore GNSS displacements are comparable in amplitude to some of the largest
137 offshore Gisborne SSEs observed in 2010 (Wallace and Beavan, 2010) and 2014 (Wallace et al.,
138 2016). Small differences in the displacement patterns exist, such as ~5 mm less subsidence and
139 up to 10 mm more eastward motion at GNSS sites along the Gisborne coast in 2019 compared to
140 2014, indicating that the 2019 SSEs may have had a slightly different slip distribution compared
141 to previous SSEs. Onshore GNSS site displacements in the Hawkes Bay area during the
142 April/May period (see CKID and MAHI GNSS sites) are similar to amplitudes produced by

143 previous large events in 2013, 2014/2015, and 2016 (Wallace and Eberhart-Philips, 2013;
144 Wallace et al., 2017).

145 Instruments from the 2018/2019 seafloor geodetic and seismic experiment offshore
146 Gisborne and Hawkes Bay (Barker et al., 2019) were recording during the 2019 SSE (Woods et
147 al., 2022), in addition to two IODP observatories offshore Gisborne (Wallace et al., 2019). The
148 temporary APGs from the seafloor experiment and the pressure sensors at the wellhead of the
149 observatories form two clusters of five seafloor pressure sensors offshore (a) Gisborne and (b)
150 beneath Hawke Bay (see purple circles in Supplementary Figure 1b). Three of the APGs beneath
151 Hawke Bay contained the new A-0-A technology (e.g., Wilcock et al., 2021), to mitigate drift of
152 the pressure sensor, which can be up to several cm/yr (Polster et al., 2009). Woods et al. (2022)
153 processed the pressure timeseries including drift correction, and utilizing reference pressure sites
154 outside of the SSE regions and Ocean Global Circulation Models (OGCMs) to correct for
155 regional oceanographic variations. The processed data revealed that there was 10–33 mm of
156 seafloor uplift offshore Gisborne associated with the 2019 SSE, and 11–27 mm uplift beneath
157 Hawke Bay (Figures 1b, 1c).

158 The onshore GNSS timeseries (MAKO, near Gisborne) indicates that the SSE starts
159 offshore Gisborne in early April/late March and lasts until the end of April, consistent with the
160 timing of uplift observed in the APG data offshore Gisborne, although the APG data (particularly
161 at near-trench sites KU18-2 and U1518) indicate the event likely persisted near the trench until
162 mid-May. Hawkes Bay GNSS sites suggest the SSE at central Hikurangi lasted from early April
163 to early June, although the seafloor pressure changes at sites near the trench (see LBPR18-4 and
164 POBS18-3) suggest that SSE may have persisted near the trench at central Hikurangi until mid-
165 July (Figure 1; Woods et al., 2022). These delayed near-trench displacements could be due to
166 trenchward migration of the SSE beneath Hawke Bay over the late-May-July period, which is
167 not possible to detect with the shore-based GNSS network. To characterise shallow subduction
168 interface slow slip during the 2019 SSEs, we invert continuous GNSS data, InSAR LOS
169 displacements, and seafloor pressure time series (as a proxy for vertical displacement of the
170 seafloor) for time-dependent slip on the subduction plate boundary.

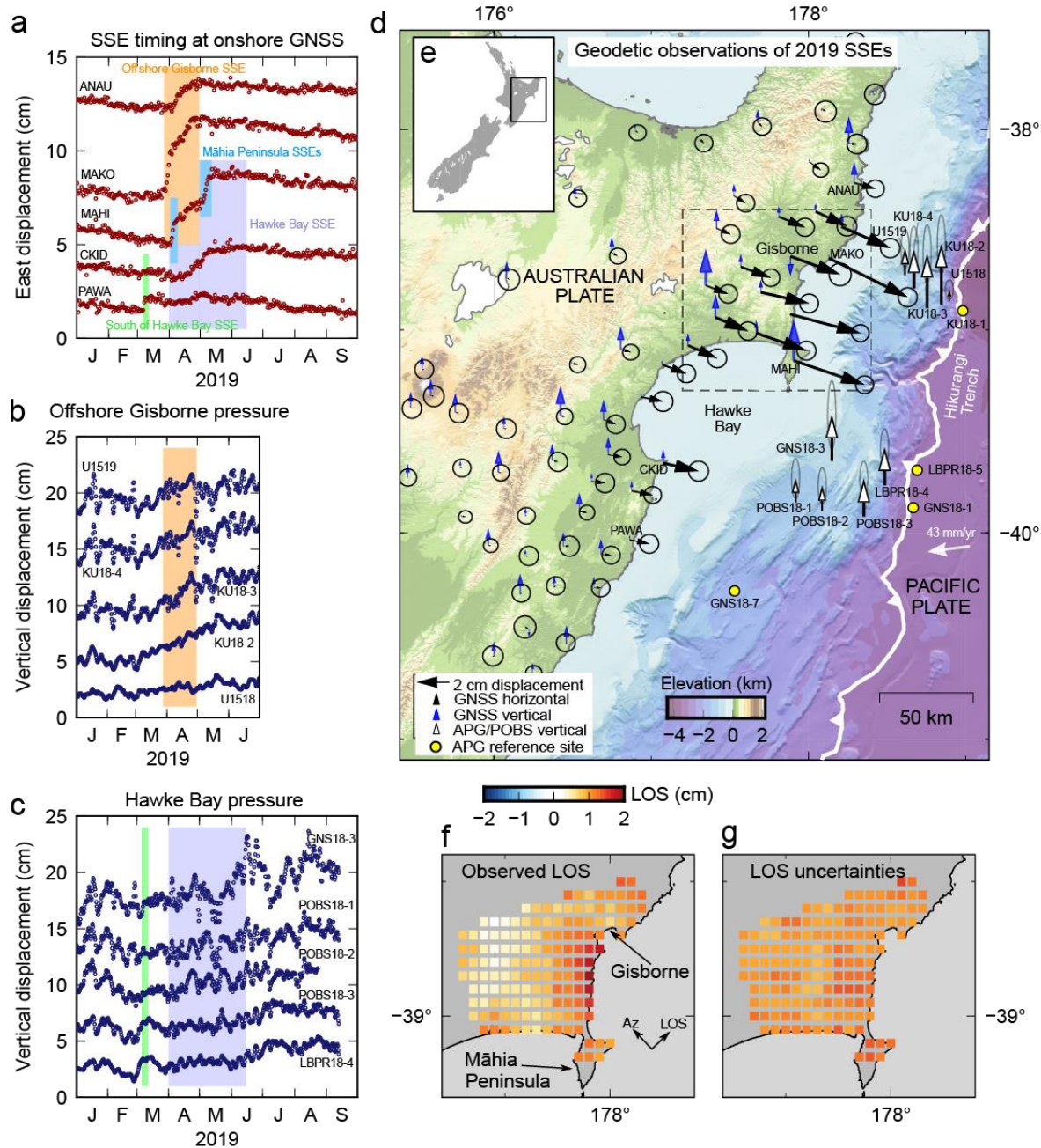


Figure 1: Onshore and offshore geodetic observations of the 2019 SSE sequences at the shallow Hikurangi subduction zone. *a*) East component timeseries of GNSS sites (relative to ITRF2014, and offset in the vertical axis to make each signal clear) with the period of detected SSEs highlighted for each site; site locations shown on *(d)*. *b*) The vertical timeseries data estimated at the Gisborne seafloor pressure array (Woods et al., 2022), with SSE timing from onshore GNSS in *(a)* indicated by orange shading. *c*) Vertical displacement timeseries data from the Hawke Bay seafloor pressure array (Woods et al., 2022), with SSE timing detected by onshore cGNSS stations indicated by lavender shading. *d*) Horizontal and vertical GNSS displacements (and site locations) over the 2019 SSE period. The motion of the Pacific

180 plate relative to the Australian plate is denoted with a white arrow (Beavan et al., 2002). Reference APGs
181 used in the processing of the seafloor pressure data are plotted as yellow circles. f) InSAR LOS
182 displacements, following the convention that a positive displacement is motion away from the satellite. As
183 the SSE motion is primarily eastward motion, it is detected as an LOS increase (motion away from the
184 satellite). g) InSAR LOS displacement uncertainties.

185 **3 Onshore and offshore geodetic data**

186 **3.1 GNSS Time Series**

187 We include the daily, three-component GNSS time series (acquired and processed by GeoNet,
188 and available at www.geonet.org.nz) of 64 stations along the east coast and central part of North
189 Island (see red triangles in Figure S2 in the Supplementary material) from 1 January 2019 to 1
190 October 2019 (Figure 1a). The data span the SSE period and several months before and after the
191 SSE to allow inter-SSE motion of the GNSS stations to be estimated during the inversion.
192 The GNSS time series provide critical spatiotemporal information about the SSEs (for slip
193 occurring within observable range of the onshore network), such as the onset and termination of
194 slow slip, and periods and general locations hosting the most rapid slip. Prior to inverting the
195 data, offsets due to equipment changes are corrected for in the GNSS time series.

196 **3.2. InSAR LOS Displacements**

197 InSAR LOS change data acquired before and after the SSE improves the onshore spatial
198 resolution of deformation for the Gisborne region. We generate a small baseline network of
199 interferograms spanning the Gisborne region from August 2014 to November 2020 (19 strip map
200 acquisitions from an ascending track 99 of the ALOS-2 mission) using the GAMMA processing
201 software (Werner et al., 2000), which are then input into StamPS (Hooper, 2008; Hooper et al.,
202 2012) to generate small baseline interferograms. Topographic corrections are applied using the
203 ALOS Global Digital Surface Model (30 m horizontal resolution; Tadono et al., 2014; Takaku et
204 al., 2014, 2016; Tadono et al., 2016; Takaku and Tadono, 2017; Takaku et al., 2018, 2020).

205 The SSE deformation is expected to produce a long wavelength signal across the interferogram,
206 which makes a correction of long wavelength atmospheric or orbital signals using a ramp more
207 challenging as the ramp would also remove the deformation signal. Using predicted LOS
208 displacements, generated by a preliminary SSE model constrained by GNSS sites only, we

209 subtract the SSE deformation signal, fit and subtract a ramp representing remaining
210 atmospheric/orbital gradients, and add the predicted deformation back into the interferogram
211 (similar to the approach of Hamling et al., 2022).

212 We confirm that the LOS displacement time series is consistent with the onshore GNSS motion
213 in the area, particularly over the February 2019 – July 2019 period we are investigating
214 (Supplementary Figure S3). The resolved 2019 SSE displacement field from the InSAR (see
215 Supplementary Figure S4) is then sub-sampled so the density of data points are reduced, and the
216 locations align with the locations of Green's functions generated for the inversions (see Section
217 4.0). The resultant LOS displacements can be seen in Figure 1f, where positive changes represent
218 motion away from the satellite — positive LOS changes are equivalent to eastward, northward,
219 and downward (subsidence) motion. A maximum of ~20 mm LOS displacement is detected at
220 the coast near Gisborne, decaying to <5 mm detected displacement ~50 km inland; we note that
221 uncertainties in the LOS displacements generally range from 5-10 mm (Figure 1g).

222 **3.3 Seafloor Pressure as a Proxy for Seafloor Vertical Displacement**

223 The onshore GNSS data provide good temporal and spatial resolution for SSE slip near and
224 below the coast; however, these data lose revolving power for the offshore (< 12 km depth)
225 portions of the subduction zone (see Section 1.0 of the Supplementary Material). To constrain
226 vertical displacement of the seafloor, we use continuous recordings of seafloor pressure (using
227 Absolute Pressure Gauges, or APGs) deployed during the 2019 SSE to better constrain the
228 offshore slip distribution (see processed timeseries from Woods et al., 2022, in Figures 1b and
229 1c).

230 The processing of the seafloor pressure data is outlined in detail in Woods et al. (2022), and we
231 summarize the key components of this below. Our procedure first involved the removal of high
232 frequency signals (such as diurnal and semidiurnal tides) using a 2-day corner lowpass filter, and
233 then a correction for instrumental drift of the APGs equipped with ambient-zero-ambient (A-0-
234 A) technology. After low-pass filtering, significant non-tidal oceanographic signals remain with
235 amplitudes on the order of a few to ten cm, which will mask any pressure changes due to vertical
236 tectonic deformation (which we expect to be on the order of a few cm). Similar to previous
237 studies (Wallace et al., 2016; Frederickson et al., 2019; Inoue et al., 2021) which assume a large
238 component of these non-tidal signal are common-mode across the footprint of the array, we

mitigate this noise by subtracting the pressure record of an APG located outside the expected SSE deformation region. The Gisborne APG array reference site was located on the subducting plate (KU18-1) and a composite reference site (consisting of an APG located along-strike (GNS18-7) and the average of two subducting plate APGs (GNS18-1 and LBPR18-5)) was used for the Hawke Bay array (see Fig. 1d for reference site locations; Woods et al., 2022).

A further correction was then included to account for contributions from long-period ocean variability between the reference sites and main arrays. This involved subtracting the weighted average of 90-day window moving mean simulated pressure time series representing the oceanographic variations between each APG and reference site. The simulations were generated using the global Ocean General Circulation Models (OGCMs): ECCO2 (Estimating the Circulation and Climate of the Ocean project; Menemenlis et al., 2008), GLORYS (GLObal Ocean ReanalYsis and Simulation; Lellouche et al., 2021), and HYCOM (HYbrid Coordinate Ocean Model; Cummings, 2006; Cummings and Smedstad, 2013; Helber et al., 2013), with the weighting of each OGCM determined by the cross-correlation of the observed and simulated pressure data. Following the ocean noise corrections, the APGs not equipped with A-0-A self-calibration, were drift-corrected by fitting a linear function to data outside the period of slow slip (indicated by the onshore GNSS data in Figure 1a), which was subtracted from the APG time series.

The seafloor pressure data are processed using 1-hour sampling and then sub-sampled to a 4-hour average value for input to the time-dependent inversion. Vertical displacement time series at ten offshore locations are included, from 1 January to 1 October 2019 for Hawke Bay APGs, and from 1 January to 1 July 2019 in the Gisborne region (with post-July data excluded due to the presence of large amplitude, winter ocean noise — confirmed with the seafloor pressure simulations from the OGCMs).

4.0 Time-dependent inversion of the onshore and offshore geodetic data for slip on the megathrust

To resolve the spatial distribution and temporal evolution of the 2019 SSE sequence, we use the non-linear, time-dependent inversion software TDEFNODE (McCaffrey, 2009). The three-component GNSS time series, InSAR LOS displacements, and seafloor vertical displacement time series data (Table 1) are inverted for eight transient slip sources characterising the 2019

269 slow slip event sequence (see Tables S1 and S2 in the supplement for a summary of the source
270 parameters and constraints on the source parameters).

271 The TDEFNODE inversion framework includes a set of tectonic blocks, each with a different
272 Euler pole of rotation and boundaries represented by known active faults (Supplementary Figure
273 S2; Wallace et al., 2004, 2012a). We define the Hikurangi subduction interface using a grid of 24
274 by 11 nodes extracted from the interface geometry of Williams et al. (2013), along which the
275 SSE transients are assumed to occur. We use the poles of rotation of Wallace et al. (2012a) and
276 the plate boundary geometry to fix the rake of slip to reduce the number of free parameters
277 solved for in the inversion.

278 To relate surface displacement at the onshore and offshore geodetic sites to slip on subduction
279 megathrust patches, we generate our own Green's Functions using the finite element code PyLith
280 (Aagaard et al., 2013; 2017a; 2017b). This allows us to account for spatially variable elastic
281 properties, following the method of Williams and Wallace (2015). Most crustal deformation
282 models to fit geodetic data assume dislocations in a homogeneous elastic half-space, utilizing
283 analytical equations that relate fault slip to surface displacement (Okada, 1985). By undertaking
284 inversions of geodetic surface displacements for slip on the megathrust using realistic elastic
285 properties (constrained by seismic velocities) at the Hikurangi subduction zone, Williams and
286 Wallace (2015, 2018) demonstrate that the assumption of homogeneous elastic properties results
287 in an under-estimation of slip for offshore Hikurangi SSEs (by up to 70%), and an
288 overestimation of slip (by up to 20%) for deep Hikurangi SSEs. This has important implications
289 when trying to understand the role of SSEs in accommodating the plate motion budget. To
290 account for heterogeneity of elastic properties in the deformation models, we use Green's
291 functions relating surface deformation response to slip on all patches with elastic properties
292 constrained by the New Zealand-wide seismic velocity model (Eberhart-Phillips et al., 2010;
293 Eberhart-Philips and Bannister, 2015; Eberhart-Phillips and Reyners, 2012; Reyners et al., 2014).

294 The time-dependent inversion code TDEFNODE (McCaffrey, 2009) has the advantage of
295 reducing the number of free parameters by representing spatiotemporal slip evolution as more
296 simplified basis functions, rather than inverting directly for slip (or slip rate) on discrete fault
297 patches during individual time steps. This removes the need for extensive regularization and
298 smoothing that must be implemented in some other time-dependent inversions (such as the

299 Network Inversion Filter; Miyazaki et al., 2006; Bartlow et al., 2011). Here, SSE transients are
 300 represented through basis functions in space and time. The slip distribution is characterised using
 301 a 2D Gaussian function:

$$302 \quad S(x, w) = Ae^{-0.5\left(\frac{dw}{d_1}\right)^2} e^{-0.5\left(\frac{dx}{d_2}\right)^2}, \quad (1)$$

303 where $S(x, w)$ represents the spatial slip distribution (x is the along-strike position and w is the
 304 along-dip position) as a function of the amplitude (A), Gaussian down-dip and along-strike width
 305 of the source ellipse (d_1 and d_2), and the down-dip and along-strike distance (dx and dw) from a
 306 node to the Gaussian mean (longitude and latitude of the centre of the slip source). The transient
 307 time history is characterised with a Gaussian temporal function:

$$308 \quad S(t) = Ae^{\frac{(t-(T_o+3T_c))^2}{T_c}}, \quad (2)$$

309 where T_c is the transient time constant (a measure of duration) and T_o , the transient origin time.
 310 $T_o = T_{max} - 3T_c$, where T_{max} is the time of peak slip rate.

311
 312 The number of transients resolved in the TDEFNODE inversion must be pre-defined. Eight
 313 transients (i.e., eight SSE transient sources, see Table S2 in the Supplement) were chosen by
 314 visually inspecting the GNSS and APG time series and identifying the number of phases of slow
 315 slip based on the onset, duration, and location of SSE signals along the margin (see Figures 1a,
 316 1b, and 1c). An exception to this classification is the first period of rapid motion detected at
 317 Māhia Peninsula (see early April SSE signal at MAHI in Figure 1a), which we do not model as
 318 very few other sites recorded that phase of deformation, as it would be largely constrained by a
 319 single GNSS site on Māhia Peninsula. The SSE transient sources are stationary in space in the
 320 TDEFNODE inversion, and we effectively capture the SSE migration along the interface by
 321 superimposing multiple transient sources with different spatial and temporal characteristics.

322 In addition to the SSE transient source model parameters, we solve for 6-monthly and yearly
 323 seasonal trends in the vertical component of the GNSS time series as these are larger amplitude
 324 than the vertical tectonic signals (horizontal-component seasonal signals are less obvious in the
 325 time series). We also solve for the inter-SSE rates of the three components of most GNSS sites.
 326 The inversion struggles to estimate the inter-SSE velocity of the north component at a few of the

327 GNSS sites (orange triangles in Figure S2 in the Supplement), therefore this component of those
 328 sites is fixed to the rates calculated by Wallace et al. (2012b), estimated from a longer timeseries
 329 of data.

330 Multiple iterations of grid searches and downhill simplex minimisation are performed to find the
 331 set of model parameters that minimise the reduced χ_n^2 statistic plus any inversion penalties to
 332 keep parameters within physically plausible limits:

$$333 \quad \chi_n^2 = \frac{\sum \frac{r^2}{(sF)^2}}{dof}, \quad (3)$$

334

335 where r is the residual (observed data minus the best-fitting model), s is the data standard
 336 deviation, F is a scaling factor applied to each data file, and dof is the number of degrees of
 337 freedom (64,643: the total number of data points in Table 1 minus 64 free parameters). The
 338 seafloor displacement time series and InSAR data are weighted more heavily in the inversion
 339 (using the scaling factor, F , in Equation 3), compared to the GNSS time series (which artificially
 340 dominate the inversion due to the large number of data), as the InSar and Seafloor pressure
 341 datasets contain fewer data points. More information on the inversion procedure can be found in
 342 section 2.0 of the Supplementary material).

343

344 **Table 1:** Summary of geodetic data inverted to resolve the 2019 SSEs. Information includes the type of geodetic
 345 data inverted, the source of the data processing, displacement information (e.g., east–E, north–N, up–U, Line-of-
 346 Sight–LOS), the number of sites and data points in the dataset, the time period covered, and the weighting factor
 347 used in the inversion.

Data type	Source of processing	Displacement information	Number of sites	Number of data points	Time period	Inversion weighting
Continuous GNSS	GeoNet	E N U	64	51,513	1 Jan 2019 – 1 Oct 2019	1
Seafloor pressure	Woods et al., 2002	U	10	13,050*	1 Jan 2019 – 1 Oct 2019	0.25
InSAR	This study	LOS	-	144	1 Jan 2019 – 1 Aug 2019	0.05

348 *8,700 simulated noise (horizontal component) and 4,350 real data points.

349

350 **5.0 Results**

351 The overall slip distribution resolved by our time-dependent inversion of onshore and offshore
352 geodetic data is shown in Figure 2. Our best-fitting solution has a reduced χ_n^2 value of 1.21, and
353 generally fits the onshore and offshore data to within uncertainty. The slip distribution includes
354 two main loci of slip, one reaching 150–200 mm offshore Gisborne at 6–9 km depth, and the
355 other reaching >200 mm slip at 9–12 km depth beneath Hawke Bay. These large slip patches
356 appear to be separated by a region of low amplitude slip offshore Māhia Peninsula, although the
357 lower inferred slip between the two primary slip patches may also be due to the lack of offshore
358 observations between the two seafloor arrays, where the model is not well-resolved (see spatial
359 resolution tests in Section 1.0 of the supplemental material). Substantial spatiotemporal evolution
360 of the event is evident in the onshore and offshore geodetic timeseries (Figure 1), which we
361 discuss in detail in sections 5.1 and 5.2.

362 The observed onshore and offshore displacements for the entire SSE period of February–July
363 (including the short burst of slow slip offshore southern Hawkes Bay in February), are fit well by
364 the slip model in Figure 2. Although most timeseries are fit very well for all sites (see
365 Supplementary Section 4.0 for fits to all timeseries), the north component of the MAHI GNSS
366 station on Māhia Peninsula is not as well-fit with our best-fitting model (Figure 3). The misfit
367 may be a result of inaccuracies in the physical assumptions made in the inversion, such as
368 prescribed direction of slip, the subduction interface geometry, and elastic properties. However,
369 we expect that this misfit is more likely related to needing a more complex slip model than can
370 be captured in the TDEFNODE inversions without addition of more free parameters. We will
371 examine the Gisborne and Hawkes Bay regions separately to highlight features of the slip model
372 for those two regions.

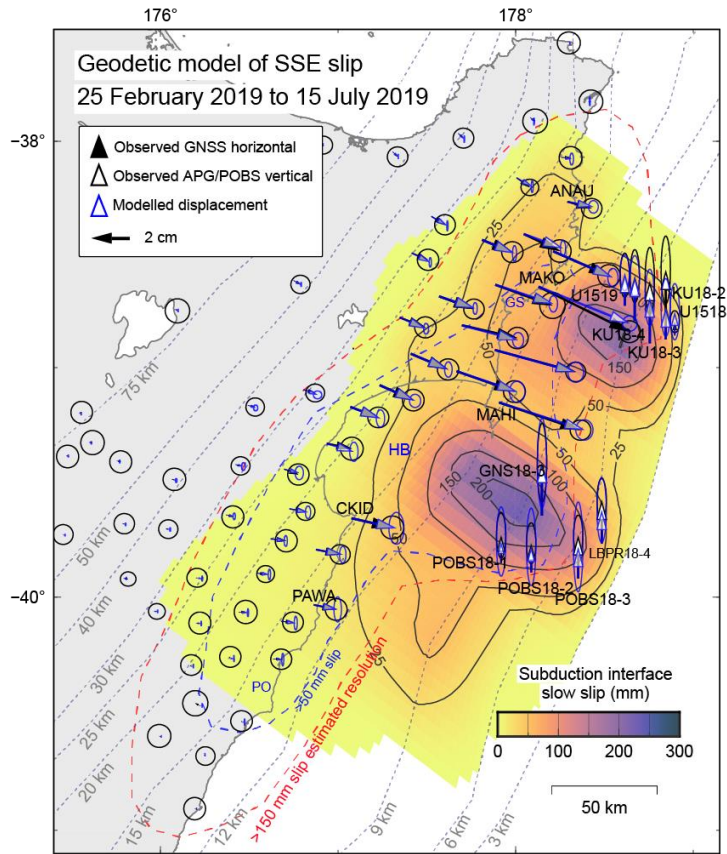
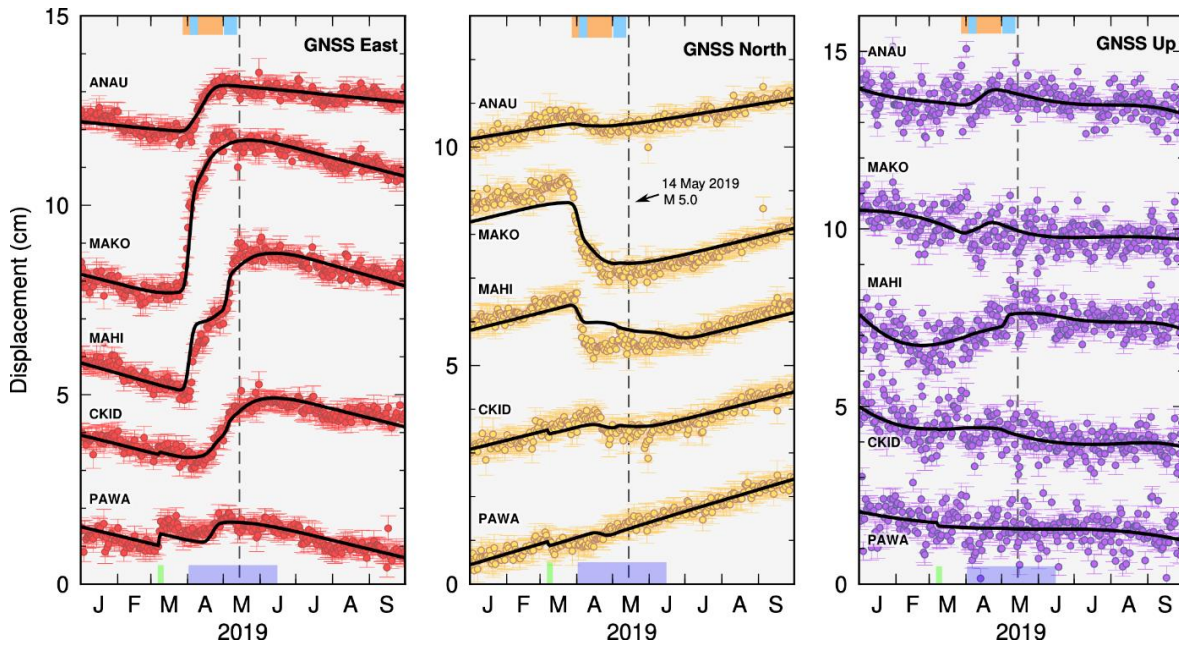


Figure 2: The best-fitting subduction interface SSE slip distribution from 25 February 2019 to 15 July 2019 in millimetres (see color scale). Solid black vectors indicate observed onshore total horizontal displacement during the SSE period and black outlined vectors are the observed offshore vertical displacement (Woods et al., 2022). Blue outlined vectors show the displacement from the best-fitting slip distribution. Grey dashed contours denote the depth to the subduction interface (labeled in km) (Williams et al., 2013). The estimated model resolution, for >50 mm and >150 mm of slip, is indicated with blue and red dashes respectively (based on the spatial resolution tests in Supplementary Material section 1.0). The locations of Gisborne (GS), Hawke Bay (HB), and Pōrangahau (PO) are also shown.

5.1. Slow slip offshore Gisborne

Our model does a reasonable job capturing the rapid and more gradual phases of the Gisborne SSE motion evident in the onshore GNSS timeseries (see ANAU and MAKO east component time series in Figure 3, and fits for all other GNSS and APG sites in Section 4.0 of the Supplementary Material). The rapid early motion detected onshore from 25 March to 8 April (e.g., MAKO in Figures 2-3) is well-fit by SSE slip of ~65 mm over 11 days, on a ~55 km by ~80 km patch located along the interface located immediately seaward of the Gisborne coastline,

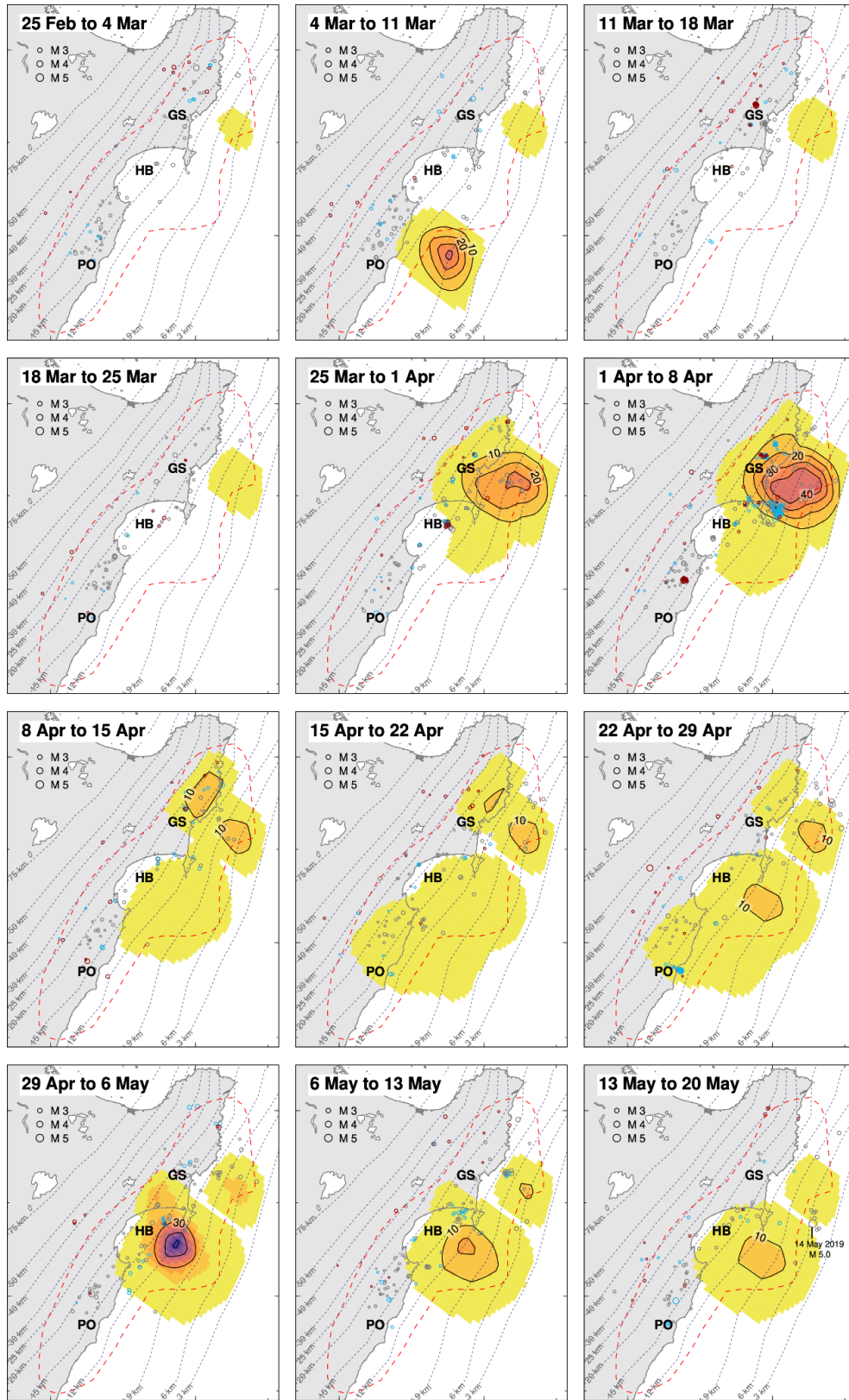
389 northeast of Māhia Peninsula (also see Figure 4). It is during this rapid early phase that small to
 390 moderate earthquakes are the most abundant, particularly along the southern edge of the slipping
 391 patch, with locations close to the plate interface (Figure 4, see 1-8 April panel). As the APG data
 392 are noisier than the onshore GNSS timeseries, a similar rapid uplift signal during this rapid early
 393 phase is not obvious, but there was an overall uplift/pressure decrease signal at all APGs through
 394 the entire duration of the SSE, with 10–33 mm of estimated uplift (Figure 5; Woods et al., 2022).
 395 To fit both the APG data and GNSS timeseries, our models suggest a second, longer-lived (early
 396 April to mid May) phase of slip immediately following and updip of (at 6-9 km depth) the initial
 397 rapid 11-day pulse (Figure 4). This characterises the temporal signature of the APG vertical
 398 displacement time series well, and also fits the onshore GNSS timeseries during this period. This
 399 suggests that while there was more rapid slow slip detected onshore occurred close to the coast
 400 (between 25 March and 8 April), there was also a more gradual patch of larger slow slip centred
 401 further up-dip (between early April and mid to late May, as seen in Figure 4) detectable in the
 402 APG data.

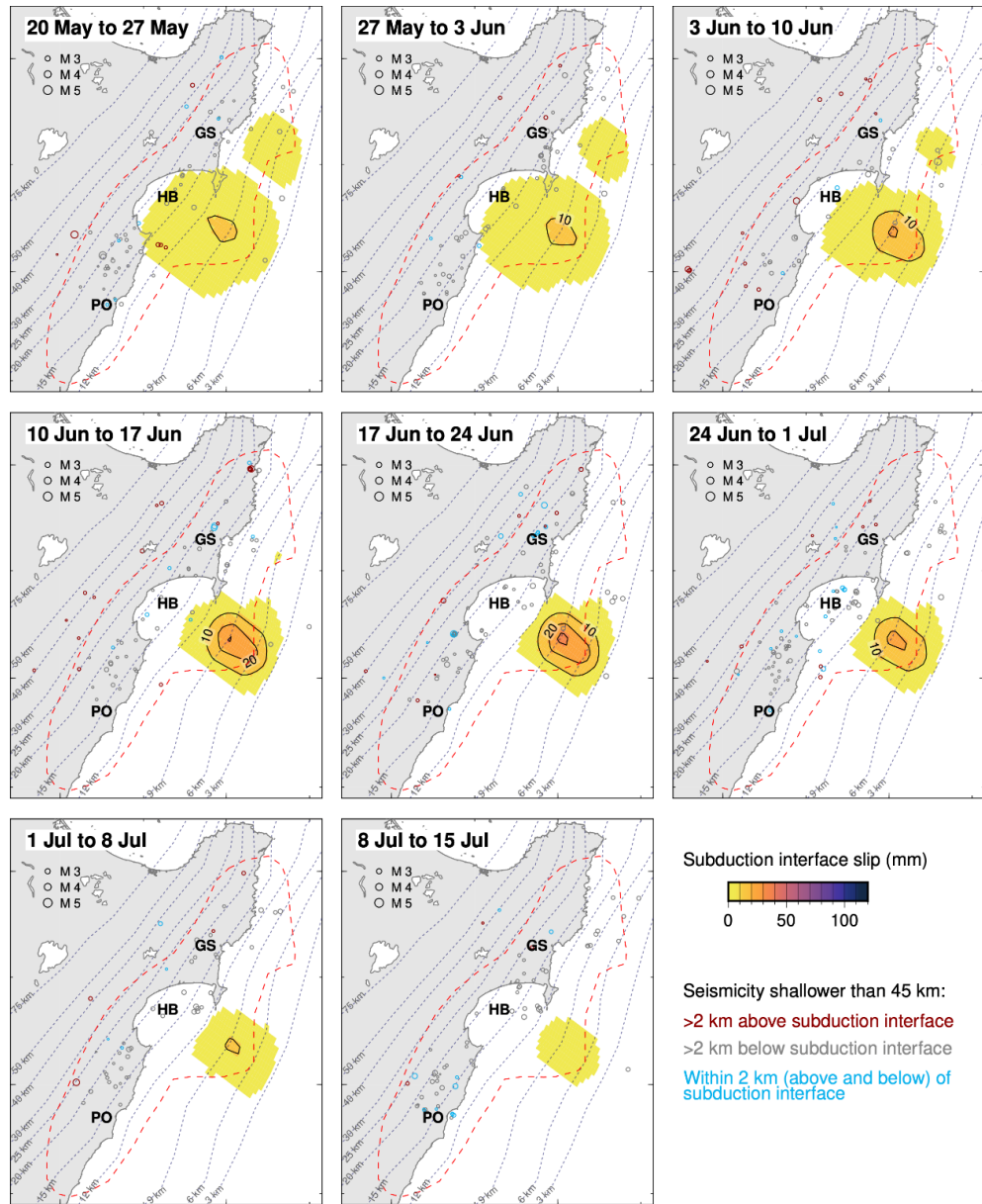


403 **Figure 3:** The observed and predicted east, north, and up GNSS timeseries for ANAU (Anaura Bay),
 404 MAKO (Makorori), MAHI (Māhia Peninsula), CKID (Cape Kidnappers), and PAWA (Pawanui; see
 405 Figure 1 for locations). The observed data are shown as red (east component), gold (north component),
 406 and purple (up component) data points, with the predicted displacement time series (from the best fitting
 407 model in Fig. 2) indicated with a solid black line. The GNSS time series shown are relative to ITRF2014
 408 and are not detrended for inter-SSE motion. The timings (discussed in the text) of SSE signals detected at
 409

410 *onshore GNSS stations are indicated (at the top of the panels) with orange shading for Gisborne*
411 *(MAKO), light blue for Māhia Peninsula (MAHI), and green and lavender shading for Hawke Bay*
412 *(PAWA and CKID respectively) at the bottom of the panels.*

413 The slip model fits the InSAR LOS displacements well (Figure 6), with LOS change residuals
414 less than 10 mm (within the LOS data uncertainties). To fit the observed, large (~40 mm)
415 onshore horizontal displacements near Gisborne, high amplitude subduction interface slip
416 beneath the offshore region is required. Due to the basis functions used in the inversion to reduce
417 the number of free parameters, (such as modelling a slip phase as a stationary transient following
418 a single temporal function), the slip model does not capture all of the detailed features of the
419 SSEs visible in the GNSS timeseries, such as slight variations in the onset time of the rapid early
420 SSE phase detected along the Gisborne coast, which may indicate some along-strike migration of
421 the event (see GISB, PARI, and MAKO time series in Supplementary Material section 4.0). In
422 addition to this, there is minor misfit to the north-component time series of ANAU and MAKO
423 (Figure 3), with the southward motion of the onshore sites under-estimated, indicating that there
424 is additional spatiotemporal complexity of the 2019 SSEs that cannot be captured by our model.
425 All time series observations and comparisons to the best-fitting model can be seen in section 4.0
426 of the Supplementary Material.





429

430 **Figure 4:** Weekly time slices of the best-fitting subduction interface SSE slip distribution from 25
 431 February 2019 to 15 July 2019 in millimetres. Seismicity detected by GeoNet
 432 (<https://www.geonet.org.nz/data/types/eq> catalogue) during the 2019 SSEs at depths shallower than 45
 433 km is presented for: earthquakes located more than 2 km above the subduction interface (dark red
 434 circles), earthquakes located more than 2 km below the subduction interface (grey circles), and
 435 earthquakes located within 2 km (above and below) the interface (blue). The estimated model resolution,
 436 for >150 mm of slip, is indicated with red dashes (determined from the spatial resolution tests in the
 437 Supplementary Material section 1.0). The locations of Gisborne (GS), Hawke Bay (HB), and Pōrangahau
 438 (PO) are also shown.

Overall, the offshore Gisborne SSE slip in 2019 appears to have ~100 mm lower peak slip than the 2014 event (Wallace et al., 2016), with the 2014 peak slip localised on the western side of the 2019 peak slip (see Figure 7). These differences can most likely be attributed to more comprehensive coverage of the seafloor APGs providing better constraints on the offshore slip distribution during the 2014 SSE, but could also be a result of variations between the 2014 and 2019 slip episodes. The largest seafloor vertical displacements (27–54 mm) estimated for the 2014 SSE are located close to the peak of the 2014 SSE slip. The 2019 APG network spans the northern edge of the 2014 SSE slip distribution (approximately 20 km north of the region of peak slip). For the sites from the 2014 HOBITSS experiment that are in similar locations to our 2019 Gisborne APGs, we see a 3–8 mm difference in vertical displacement estimates when comparing the 2014 and 2019 SSEs (Woods et al., 2022; Figure 7), which is a small difference and can likely be attributed to a combination of slightly varying slip distributions, seafloor instrument locations, and/or pressure data processing techniques. Due to the similarity in the 2014 and 2019 onshore and offshore displacement patterns, we infer that the 2019 SSE offshore Gisborne could have involved higher peak slip (possibly as large as the 2014 SSE); however, we don't have sufficient coverage overlying the regions of largest slip to resolve this.

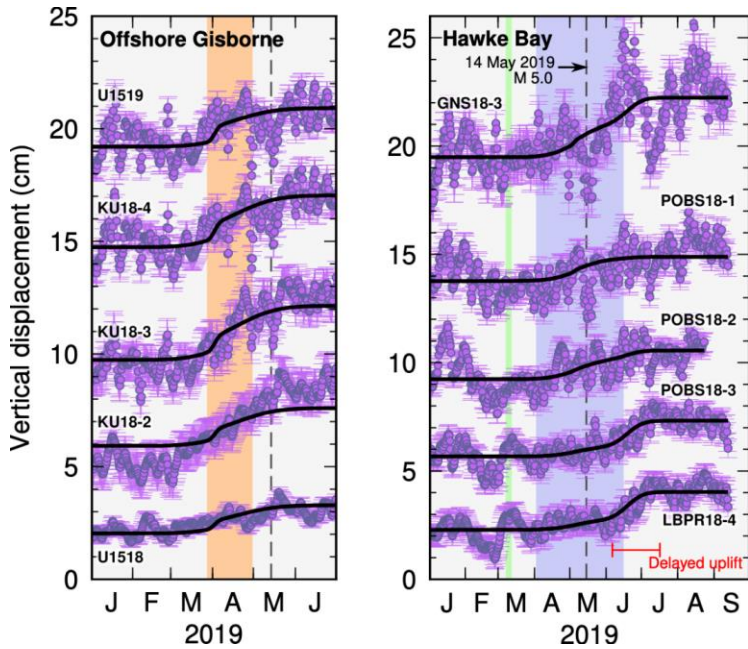
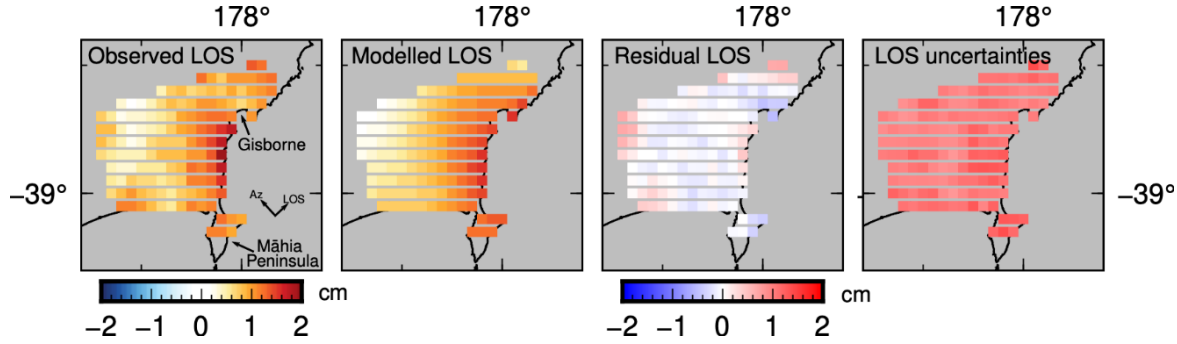
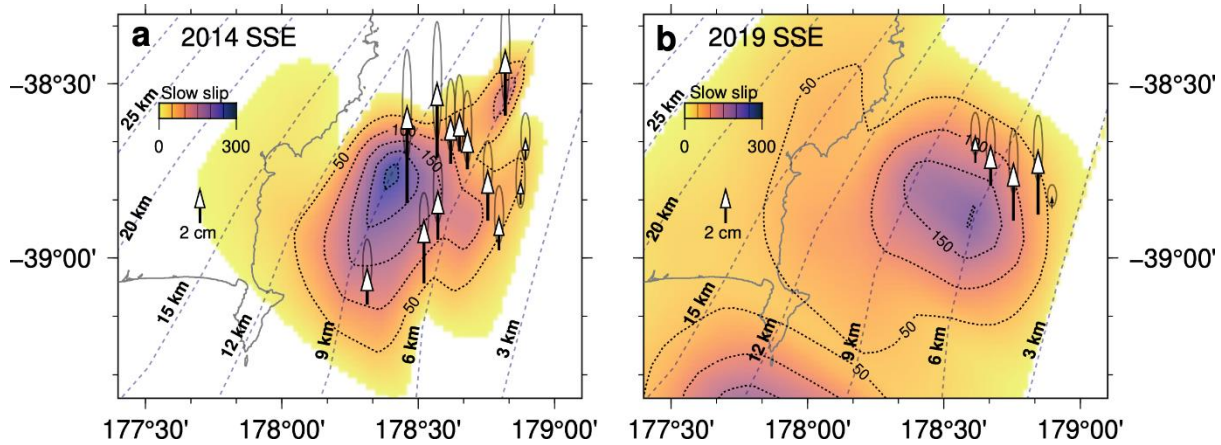


Figure 5: The observed and predicted seafloor vertical displacement timeseries, of the Gisborne APGs (left) and Hawke Bay APGs (right). The observed data are shown in purple and the predicted displacement time series (based on our best-fitting model) are indicated with solid black lines. The timing of onshore GNSS-detected SSE signals discussed in the text are indicated with orange shading for

460 *Gisborne (MAKO), and green and lavender shading for Hawke Bay (PAWA and CKID respectively). The*
 461 *site locations can be seen in Figure 1.*



462
 463
 464 **Figure 6:** Observed, modelled, residual (observed minus modelled), and uncertainty of InSAR LOS data
 465 in centimetres, with the convention that a positive displacement is motion away from the satellite. This
 466 means that subsidence and eastward and northward motion appears as a positive LOS displacement.



467
 468
 469 **Figure 7:** Offshore vertical displacement and slip distribution comparison between the 2014 and 2019
 470 Gisborne SSEs. a) the 2014 SSE slip distribution with contours in millimetres, and the offshore vertical
 471 displacement estimated by Wallace et al. (2016). b) the 2019 SSE slip distribution with contours in
 472 millimetres, and offshore vertical displacement by Woods et al. (2022). Subduction interface depth
 473 contours are indicated in kilometres (Williams et al., 2013).

474 5.2. Slow Slip offshore Hawke Bay

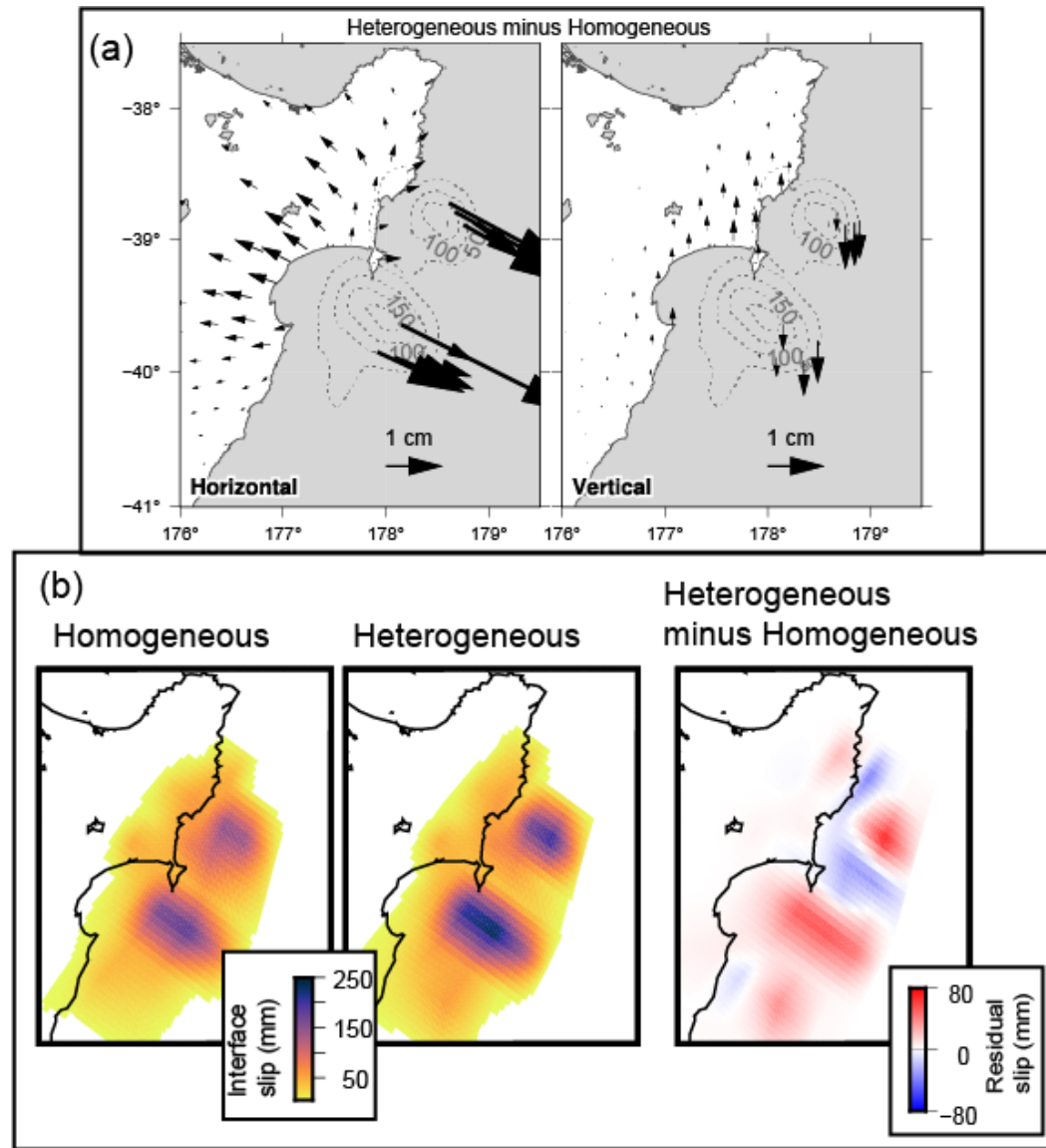
475 Slow slip appears to evolve substantially offshore the Hawkes Bay region over the March to July
 476 period. Our model indicates that the 2019 SSE sequence began with a small patch of ~30 mm of
 477 slow slip in the offshore region south of Hawke Bay between 4 March and 11 March (Figure 4),
 478 where a small eastward displacement (<5 mm) was detected at the PAWA GNSS station (Figure

479 3), which is fit as up to 20-30 mm of slip at 9 km depth. We note that our best-fitting model
480 under-estimates the eastward motion at PAWA at the beginning of March and then attempts to
481 compensate for this misfit to the time series by over-estimating the slip amplitude at the southern
482 extent of the main Hawke Bay SSE slip in April/May 2019 (Figure 3). The spatial distribution of
483 the resolved slip patch during this initial phase is poorly constrained due to the lack of offshore
484 instrumentation here and the small number of onshore GNSS sites that detected the SSE (see
485 spatial resolution tests in Supplementary Material section 1.0).

486 There is a rapid (~7 days) pressure decrease (possible uplift signal) observed at seafloor pressure
487 sites LBPR18-4 and POBS18-3 during the week before the onshore signal observed at PAWA in
488 March (Figure 5). It is challenging to determine whether the rapid pressure decrease observed at
489 both sites is due to seafloor uplift (related to slip near the trench during this short-lived SSE
490 detected >100 km away at PAWA) and/or ocean noise. Our inversion struggles to find a slip
491 model that fits both onshore and offshore displacements using a single, stationary transient, and a
492 more complex slip model (with a larger number of free parameters) would be needed to fit the
493 APG data near the trench. Given the uncertainty as to whether the signals observed at the two
494 APG sites in March is tectonic or oceanographic, we do not attempt to fit this signal, although
495 we raise the possibility that the SSE observed at PAWA was preceded by a pulse of near-trench
496 slip close to sites LBPR18-4 and POBS18-3.

497 Onset of SSE-related displacement beginning in early April at Hawkes Bay GeoNet GNSS sites
498 (e.g., CKID in Figures 2 and 3) is well-fit by a ~100 km² patch of slip (up to 200 mm over ~2
499 months) centred on the offshore region due south of Māhia Peninsula. Our best-fitting model
500 suggests a patch just up-dip of this region began slipping in late May, persisting until the middle
501 of July (Figure 4). This later period of slip is constrained largely by the Hawke Bay APG data,
502 where clear pressure decrease (uplift) signals of LBPR18-4 and POBS18-3 appear delayed by six
503 weeks relative to the onset of SSE motion at the onshore GNSS stations (as shown in Figures 1c
504 and 5). Our best fitting model suggests ~130 mm of slip occurring on the shallow (4–11 km
505 depth) plate interface over a 40-day period. A small amount of eastward displacement is also
506 visible on CKID throughout this period, indicating that the cGNSS are consistent with longer
507 duration offshore slip.

508 Of the Hawke Bay APG sites, we observe the largest vertical displacements at GNS18-3 (27
509 mm; Figure 5); however, the large amplitude oceanographic fluctuations present in the GNS18-3
510 pressure data from May onward indicate that some component of this uplift signal could be
511 influenced by oceanographic effects. If the total vertical displacement estimated at GNS18-3 is
512 too large (as a result of oceanographic contributions) then the resolved subduction interface slip
513 could be an over-estimation. An inversion of the 2019 SSEs constrained using only the onshore
514 instrumentation suggests that 60–70 mm of subduction interface slip south of Māhia Peninsula
515 explains the SSE motion detected onshore; however, the onshore GNSS data provide little to no
516 resolution for the portions of the interface within 20–40 km of the trench, so this should be
517 considered a minimum (Figure S1 in the Supplementary Material). Given the possibility that
518 oceanographic fluctuations at GNS18-3 may lead to an overestimate of vertical displacement at
519 that site, we expect that the true value of the subduction interface slip for the 4–11 km depth SSE
520 region in late May–mid July 2019 period lies somewhere between 60 mm (using only GNSS
521 data) and ~130 mm (including APG data).



522

523 **Figure 8:** Comparison of results using homogeneous elastic properties and realistic, heterogeneous
 524 elastic properties in our slip inversions. (a) Predicted displacement differences using the our best-fitting
 525 slip distribution (Fig. 2) using heterogeneous elastic properties versus a homogeneous elastic half-space.
 526 Displacement differences are the displacements at each site from the heterogeneous elastic model minus
 527 the displacements predicted by a homogeneous model. Left: Horizontal displacement differences for
 528 onshore GNSS and offshore APG sites; vectors pointing east indicate displacements in the heterogeneous
 529 model are higher, while vectors pointing west indicate smaller displacements in the heterogeneous model
 530 compared to the homogeneous model. Right: Vertical displacement differences for onshore GNSS and
 531 offshore APG sites, with vectors pointing up meaning higher displacement in the heterogeneous model
 532 compared to the homogeneous model, and vectors pointing down meaning lower displacement in the
 533 heterogeneous model. The slip model is indicated with dashed contours, in millimetres. (b) Slip

534 *distributions resolved when using a homogeneous elastic property model (Left) and a heterogeneous*
535 *elastic property model (Center). Right panel shows the slip distribution from the Homogeneous model*
536 *subtracted from the Heterogeneous model (e.g., positive values indicate higher slip amounts in the*
537 *Heterogeneous slip model).*

538 **5.3 Impact of Elastic Properties on Slip Model**

539 The large elastic property contrasts between the slab and forearc at subduction zones strongly
540 influence the resulting crustal deformation models (Williams and Wallace, 2015, 2018). To assess
541 the influence of realistic elastic properties on our slip models, we forward model the
542 displacements produced by our resolved slip distribution for the 2019 SSE using both
543 heterogeneous and homogeneous Green's functions (see description of Green's function
544 generation in Section 4 and Williams and Wallace, 2018), and calculate the difference between
545 the surface displacement patterns. (Figure 8). Using heterogeneous Green's functions predicts
546 less horizontal motion at sites located on the down-dip side of the SSE area and more horizontal
547 motion at sites located closer to the SSE source on the Gisborne coast and offshore (compared to
548 uniform elastic models, using identical slip distributions). In the vertical component, for
549 equivalent models we see that the heterogeneous assumption predicts less uplift offshore and less
550 subsidence (or more uplift) onshore (although the onshore vertical displacement differences are
551 small, <5 mm). This is consistent with the findings and synthetic 2-D models of Williams and
552 Wallace (2018), where they show the displacement differences are explained by interpreting
553 the heterogeneous contributions to the displacement field as body forces reflecting the
554 interactions of material property gradients with the strain field. These additional body forces (not
555 present in the homogeneous solution) perturb both the horizontal and vertical displacement fields
556 with respect to the homogeneous solution, yielding significantly different results for
557 homogeneous versus heterogeneous models when the same SSE slip distribution is applied to
558 both.

559 For a set of surface displacements we would therefore expect the resolved subduction interface
560 slip amplitude and distribution to vary depending on the assumptions made about elastic
561 structure. The forward-model example in Figure 8 indicates that accounting for realistic,
562 heterogeneous elastic properties produces more SSE slip (as less uplift is predicted for the same
563 amount of slip) compared to the slip distribution when assuming a homogeneous half-space.

564 Inversions using a heterogeneous or homogeneous half-space reveal that the heterogeneous
565 model estimates as much as 70–80 mm more slip along the interface beneath the offshore
566 Gisborne and Hawke Bay APG arrays (Figure 8b). This is consistent with the findings of
567 Williams and Wallace (2018), implying that the homogeneous half-space assumption leads to an
568 under-estimation of the amplitude of offshore SSE slip.

569 We compare the slip models derived using homogeneous and heterogeneous properties (Figure
570 8b) in terms of seismic potency (a measure of the size of an event), calculated by integrating the
571 slip over the slip area, which means it is independent of the material elastic property variations
572 (i.e., shear modulus). We estimate that the heterogeneous slip distribution is overall ~15% higher
573 in seismic potency than the resolved slip distribution using the homogeneous Green's functions.
574 This is a smaller difference than what Williams and Wallace (2018) found for the 2014 SSE
575 offshore Gisborne, where they calculated ~64% higher seismic potency, using the heterogeneous
576 Green's functions. Our tests indicate that less slip is resolved closer to the coast in the
577 heterogeneous model relative to the homogeneous model for the 2019 SSEs, beneath a region
578 with no seafloor pressure data. Williams and Wallace (2018) had a much larger seafloor pressure
579 dataset to constrain their slip model, meaning the 2014 SSE slip distribution is better resolved
580 than our model of the 2019 SSEs, and likely explains some of the differences we observe
581 compared to Williams and Wallace (2018). The interaction of the strain field with the gradients
582 of the material properties strongly influence the slip model results, and this will vary
583 depending on the details of the slip distribution, which may be another source of the difference
584 between our results and those of Williams and Wallace (2018).

585 **6 Discussion**

586 **6.1 Shallow SSE regions can also rupture seismically**

587 Although the rheology, frictional properties and physical processes producing episodic SSE
588 behavior is widely discussed and debated (Liu and Rice, 2007; Segall et al., 2010; Leeman et al.,
589 2016; Im et al., 2020; Shreedharan et al., 2023), many studies have suggested that regions
590 hosting slow slip events and/or steady creep are unlikely to rupture seismically (Hyndman, 2013;
591 Dixon et al., 2014; Rolandone et al., 2018). Such assumptions have propagated into seismic
592 hazard models (Petersen et al., 2020; Wong et al., 2014).

593 In contrast to common assumptions about the seismic rupture potential of SSE regions, there is
594 strong evidence for past, large subduction earthquake rupture within the source area of the
595 Gisborne and Hawke Bay SSEs. Two Mw ~7.0 earthquakes occurred in March and May of 1947,
596 located within the Gisborne SSE region (Bell et al., 2014). These events had mechanisms
597 consistent with the plate interface, and are considered “tsunami earthquakes” as they caused
598 much larger tsunami (6-10 m) than expected given their magnitude (Doser and Webb, 2003;
599 Downes et al., 2000). Along the Hawke Bay coastline, evidence for repeated meter-scale abrupt
600 coastal subsidence events (with some accompanied by tsunami deposits) are evidence for great
601 (M ~8.0) subduction interface rupture offshore the Hawkes Bay region (Clark et al., 2019;
602 Cochran et al., 2006; Hayward et al., 2015). The source of such events coincide with the source
603 of shallow Hawke Bay SSEs, such as the SSE we observed in 2019 (Fig 9). Although a recent re-
604 evaluation of these data suggests that some of these coastal deformation events may be related to
605 splay faulting in the upper plate, it is likely that at least some of these subsidence events are due
606 to subduction interface ruptures beneath Hawke Bay, or a combination of shallow subduction
607 interface rupture and splay faulting (Pizer et al., 2023).

608 The spatial coincidence of large seismic rupture and SSEs offshore Gisborne and Hawkes Bay
609 suggest that shallow SSE regions may also host hazardous seismic slip. Although onshore GNSS
610 stations have previously revealed the existence of large SSEs offshore Hawkes Bay (Wallace and
611 Beavan, 2010; Wallace et al., 2012; Wallace and Eberhart-Phillips, 2013), the data and models
612 we present here are from the first seafloor geodetic deployment to capture the distribution of
613 SSEs beneath Hawke Bay. Improved resolution of the Hawke Bay SSE region provided by the
614 offshore instrumentation indicates that SSE slip occurs between <3-15 km depth, revealing a
615 nearly complete overlap with estimates of the source area of SSEs and prehistoric Great
616 earthquakes offshore Hawkes Bay (Fig. 9).

617 Numerical modelling studies can reproduce scenarios where faults host both slow and fast
618 rupture, due to large contrasts between effective stress in the slow slip and coseismic slip zones
619 permitting the coseismic slip to extend into SSE areas (Lin et al., 2020; Ramos and Huang,
620 2019), dramatic fault weakening at high slip velocities (Di Toro et al., 2011; Tsutsumi et al.,
621 2011), or arising from fault zone geometrical complexities (Romanet et al., 2018). There is
622 observational evidence of SSE and seismic slip being hosted along the same portion of the
623 Hawaiian décollement, where regularly recurring SSEs overlap spatially with the source area of

the 2018 Mw 7.1 Hawaii earthquake (Lin et al., 2020). There are also intriguing suggestions of SSEs occurring before and potentially triggering large earthquakes, such as the 2011 Mw 9.0 Tohoku-Oki earthquake in Japan (Kato et al., 2012; Ito et al., 2013), the 2014 Mw 8.1 Iquique in Chile earthquake (Ruiz et al., 2014), and the 2014 Mw 7.3 Papanoa earthquake in Mexico (Radiguet et al., 2016), although it is not clear in these cases if regions undergoing SSE slip also slipped coseismically. Observations of coeval brittle and viscous deformation in exhumed subduction shear zones (Fagereng et al., 2019; Rowe et al., 2011), and evidence for coseismic shear heating from vitrinite reflectance and biomarker thermal maturity in near trench rocks where SSEs are also observed (Sakaguchi et al. 2011; Coffey et al., 2021) are also consistent with the possibility that shallow SSE regions can also undergo dynamic rupture.

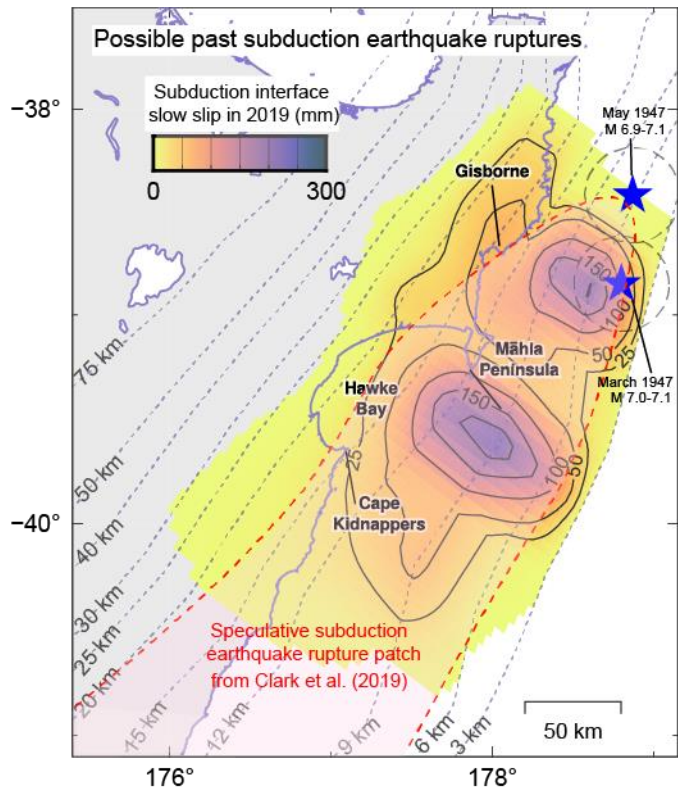
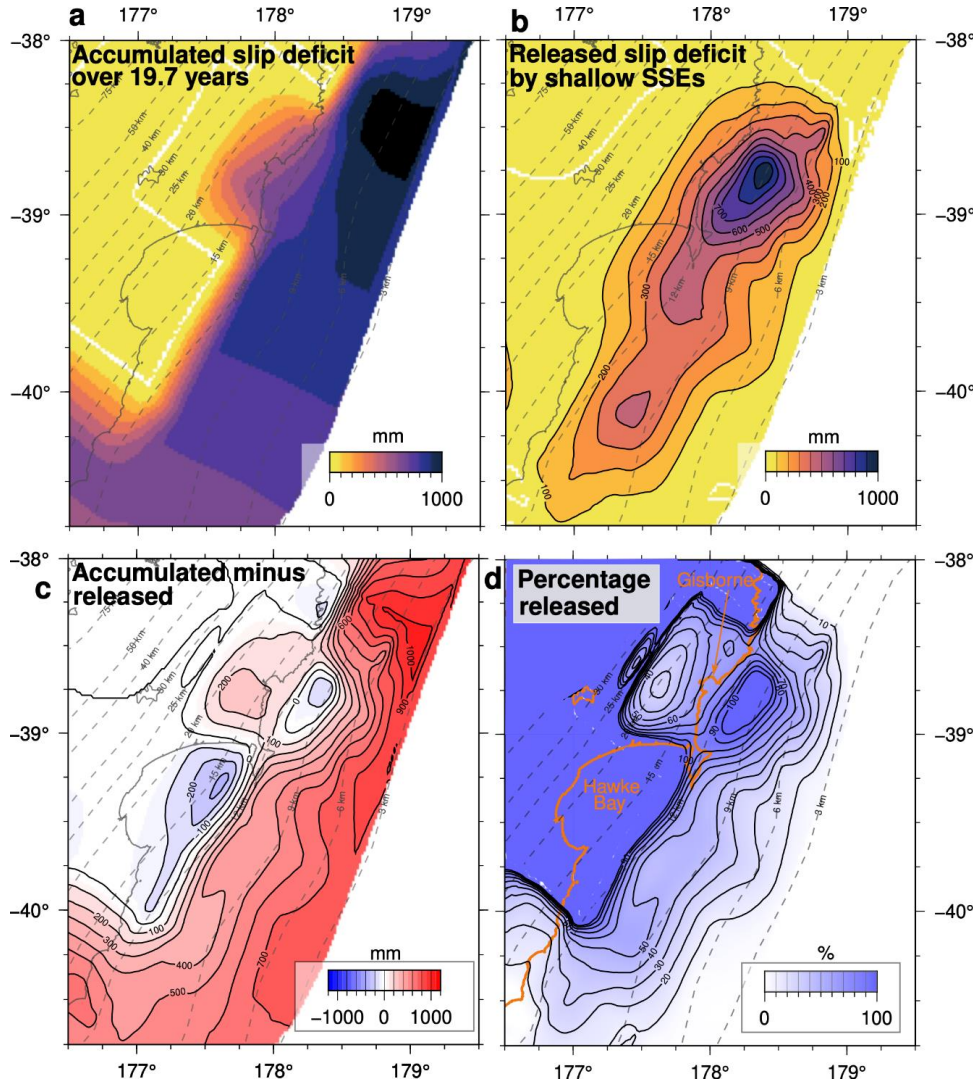


Figure 9: Slip distribution of the 2019 SSEs (black contours, in millimetres) relative to the two 1947 tsunami earthquakes (blue stars with black dashes indicating the 25 km location uncertainty; Doser and Webb, 2003; Bell et al., 2014) and the speculative subduction zone earthquake rupture patch (outlined by red dashed lines) estimated by Clark et al. (2019). Grey dashes show the depth to the subduction interface, extracted from the geometry determined by Williams et al. (2013).

Whether SSE regions are also prone to seismic rupture has important implications for our understanding of the temporal evolution of slip throughout multiple earthquake cycles at

642 subduction zones, and for quantifying the seismic and tsunami hazard posed by subduction
643 zones. Hazard models relying heavily on interseismic estimates of slip deficit rate (to define
644 locations and rates of future ruptures) for subduction megathrusts may under-estimate the
645 seismic and tsunami potential of regions dominated by SSEs and/or creep. Seismic slip could
646 also penetrate into SSE regions, increasing the area, and therefore magnitude, of the rupture (Lin
647 et al., 2020). We expect that this could be the case for the Hawkes Bay region, which is adjacent
648 to the deeply coupled southern Hikurangi margin (Fig. 9; Wallace, 2020). It is plausible that
649 ruptures initiated at southern Hikurangi could propagate into the Hawke Bay region, with the
650 large dynamic stress changes pushing the Hawke Bay SSE region to seismic failure. Indeed,
651 Clark et al. (2019) identified possible paleoseismic evidence for possible ruptures spanning the
652 southern and central segments of the Hikurangi subduction zone.

653



654
655 **Figure 10:** Released slip deficit between April 2002 and March 2022. a) The accumulated slip deficit on
656 the subduction interface in 19.7 years (April 2002 to March 2022 minus the large amplitude SSE periods
657 - approximated as ~10 weeks), based on the slip deficit rates accruing between slow slip events from
658 Wallace and Beavan (2010). b) Released slip deficit by large SSEs from 2002 to March 2022 (summing
659 the 2002–2014 SSE slip distribution of Wallace (2020), the 2014 Gisborne SSE slip distribution of
660 Wallace et al. (2016), and the 2019 SSEs resolved in our study). c) The accumulated minus released slip
661 deficit, where blue areas indicate SSEs have released more than has been accumulated in the ~20 year
662 period and red areas are where slip deficit remains. d) The percentage of slip deficit SSEs have released
663 since April 2002. However, until the last several years, there were no seafloor geodetic constraints on the
664 distribution of slip on the shallow plate boundary (<6-9 km depth), so the percentage of slip deficit
665 released for the shallow interface (<9 km) may be severely underestimated on panels c and d.

666 **6.2. Contribution of shallow SSE slip to the plate motion budget at north and central**
667 **Hikurangi**

668 Understanding the role that SSEs play in the accommodation of the plate motion budget is
669 required to address which proportion of the plate motion budget may be released seismically vs.
670 aseismically. Comparing the 2019 SSE slip with the slip deficit being accumulated during the
671 time between SSEs (e.g., during the “inter-SSE” period, from Wallace and Beavan, 2010)
672 indicates that the 2019 Gisborne and Hawke Bay SSEs recovered up to 4–5 years of slip deficit
673 (Figure 10d) in the regions of peak slow slip (\sim 9 km depth). The largest Gisborne SSEs have
674 occurred in 2004, 2010, 2014, and 2019 (every 4.5–5.5 years), with smaller SSEs occurring more
675 frequently (at least every 2 years) in the period between the large SSEs.

676 With long-term convergence rates in the Gisborne region of 50 mm/yr and 40 mm/yr at the
677 trench near Hawke Bay, we estimate that in the \sim 20 years between April 2002 to March 2022,
678 that the shallow plate boundary may have accumulated up to 1 meter of slip deficit offshore
679 Gisborne, and 0.8 meters offshore Hawkes Bay. The large shallow SSEs detected and modelled
680 since April 2002 (see Wallace, 2020, and this study) have released 400–1000 mm of slip deficit
681 offshore Gisborne and 100–500 mm beneath Hawke Bay (Figure 10b). Shallow SSEs
682 immediately offshore Gisborne (at 9–12 km depth) appear to be releasing 70–100% of the slip
683 deficit accumulated during the inter-SSE periods (Figures 10c and 10d), and 40–100% of total
684 plate motion. Prior to 2014 there were no seafloor geodetic constraints for north and central
685 Hikurangi SSEs, which could lead to an underestimate of slip on portions of the plate boundary
686 >30 km offshore; thus, the total SSE slip accommodated over the last 20 years on the shallowest
687 reaches of the plate boundary (<6 –9 km depth) are likely underestimated and the remaining slip
688 deficits should be considered a maximum. These calculations also don't include some of the
689 smaller SSEs that may have occurred within the last \sim 20 years, and are another source of error
690 that may produce an over-estimate of remaining slip deficit rate. Regardless, at least for the last
691 decade, SSEs accommodate the majority of plate motion (and in some places 100% of the plate
692 motion) at the offshore northern and central Hikurangi subduction margin.

693 **6.3 Trenchward migration and longer duration of offshore slow slip events**

694 Both the Gisborne and Hawke Bay SSEs suggest along-dip migration of the 2019 SSE (Figure
695 4). This migration is most notable in the Hawke Bay portion of the 2019 SSE sequence, with slip

696 occurring at 9–12 km depth from late April to late May, with the locus of slip migrating up-dip to
697 6–9 km depth from late May to mid-July. The APG data are crucial to detect this up-dip
698 migration of the SSEs, as the near trench (<6–9 km depth) phase of slip is not detectable with the
699 onshore GNSS stations, since this is taking place 50–100 km offshore the Hawkes Bay coastline.
700 Likewise, the time-dependent model of the 2014 Gisborne SSE estimated by Yohler et al. (2019)
701 captured by the HOBITSS network also suggests that longer durations slip occurred near the
702 trench, relative to the more rapid, earlier slip along the interface close to the coastline.

703 Observations of up-dip migration of SSEs at the shallow portions of subduction zones are far less
704 common than observations of along-strike and along-dip migration of deep SSEs, primarily due
705 to the lack of seafloor geodetic observations needed to detect the offshore (up-dip) SSE slip
706 evolution. However, pore pressure changes (as a proxy for volumetric strain) detected by
707 transects of IODP CORK observatories at the shallow portions of Nankai Trough (Araki et al.,
708 2017; Ariyoshi et al., 2021) and Costa Rica (Davis et al., 2015) subduction margins suggest up-
709 dip migration may in fact be a common feature of shallow SSEs. The migration of an SSE
710 inferred by Araki et al. (2017) at the Nankai Trough has estimated up-dip propagation velocities
711 of ~0.5 km/day, based on the 11 km spacing (along-dip) of borehole observatories and their
712 approximated migration period of 3 weeks. Davis et al. (2015) estimate up-dip propagation rates
713 of ~5 km/day for an offshore Costa Rica SSE. If a patch of slow slip did migrate from the
714 interface beneath Hawke Bay to the near-trench portion of the interface, then we estimate from
715 our geodetic model that this could have occurred over the 1–3 weeks from mid-May (Figure 4),
716 with potential propagation velocities of 1–6 km/day (based on a 20–40 km up-dip change in the
717 location of the SSE slip), comparable to the Nankai and Costa Rica examples.

718 The near-trench slip occurring during the last month of the 2019 East Coast SSE offshore
719 Hawkes Bay was not clearly detectable using onshore GNSS data, although the seafloor pressure
720 data indicate that the event persisted for at least another month (well into July). This implies that
721 using onshore GNSS data alone to estimate the duration of shallow SSEs like those in New
722 Zealand (Wallace, 2020 and references therein), Costa Rica (Dixon et al., 2014), Ecuador (Vallee
723 et al., 2013) and elsewhere may underestimate the duration of shallow SSEs by as much as 50%.
724 This has important implications for shallow SSE duration estimates used in establishing
725 Moment-duration scaling relationships (e.g., Ide et al., 2007). The nature of Moment-duration
726 scaling relationships of SSEs has important implications for whether SSEs and earthquakes arise

from the same fundamental process, and there has been much controversy about this topic with many studies obtaining results with very different implications (e.g., Ide et al., 2007; Gomberg et al., 2016; Frank and Brodsky, 2019; Michel et al., 2019; Dal Zilio et al., 2020). The much longer duration of Hawke Bay SSEs than expected using only onshore GNSS indicates that the moments and durations of offshore shallow SSEs must be utilized with care in establishing such relationships, as the duration (and to some extent, the magnitude) may be severely underestimated due to observational limitations.

7 Conclusions

Using onshore continuous GNSS data, InSAR LOS displacements, and seafloor pressure as a proxy for the vertical deformation of the seafloor, we model the spatiotemporal evolution of shallow, <15 km depth, SSEs at the northern and central Hikurangi subduction zone taking place between February 2019 and July 2019. Peaks of 150–200 mm and >200 mm total slip are estimated offshore Gisborne (at 6–9 km depth) and beneath Hawke Bay (at 9–12 km depth) respectively (releasing 4–5 years of slip deficit). Insight into the vertical seafloor deformation in these regions, from seafloor pressure sensors, indicates that the slow slip may have persisted on the shallow plate interface longer than indicated by onshore GNSS stations. Seafloor pressure data from sites offshore central Hikurangi (Hawkes Bay) reveal up-dip migration of the SSE occurred over a few weeks beneath Hawke Bay, which is too far offshore to be resolvable by the GNSS network. This indicates that shallow SSEs may last longer (several weeks or more) than is detectable by coastal GNSS networks—this has important implications for our ability to robustly characterize offshore SSE durations in the absence of seafloor geodetic data. We identify overlapping source regions between the 2019 east coast SSE sequence and locations of the March Mw 7.0–7.1 1947 tsunami earthquake offshore Gisborne and past megathrust earthquake rupture beneath Hawke Bay inferred from paleoseismic investigations. This raises the need to include SSE regions in potential earthquake and tsunami sources in hazard models at subduction zones. Denser seafloor geodetic monitoring of the shallow margin is essential to better resolving the spatio-temporal evolution of offshore slip and improving our understanding of shallow subduction processes and how the present-day SSEs interact with regional seismicity and influence the potential of future seismic megathrust ruptures.

757 **Acknowledgments**

758 This research was supported by funding to GNS Science from New Zealand's Ministry of
759 Business, Innovation and Employment's Endeavour Research Fund (contract CO5X1605),
760 funding by NSF to SCW (Grant number OCE-1754929), and Japanese Government funding to
761 Univ. Tokyo, Kyoto University and Tokyo University. To our knowledge there are no real or
762 perceived financial conflicts of interest for any author. We thank the Captain and crew of the
763 R/V Tangaroa without whom this work would not have been possible.

764

765 **Open Research**

766 Seafloor pressure data used in this study (published in Woods et al., 2022) are publicly available
767 at <https://doi.org/10.5281/zenodo.5834879>. The GeoNet GNSS timeseries data are available
768 from www.geonet.org.nz.. The InSAR Line-of-Sight change data used in the modeling is
769 included in the supplementary material of this manuscript. The modeling software utilized in this
770 research (TDEFNODE) is publicly available at
771 <https://robmccaffrey.github.io/TDEFNODE/TDEFNODE.html>. All figures were generated using
772 Generic Mapping Tools (GMT 6; Wessel et al., 2013).

773

774

775 **References**

- 776 Aagaard, B., Knepley, M., and Williams, C. (2017a). PyLith v2.2.1, Computational
777 Infrastructure for Geodynamics. <https://doi.org/10.5281/zenodo.886600>, Retrieved from
778 <https://geodynamics.org/cig/software/pylith/>
- 779 Aagaard, B., Knepley, M., and Williams, C. (2017b). PyLith user manual, version 2.2.0,
780 Computational Infrastructure for Geodynamics, Davis, CA. Retrieved from
781 https://geodynamics.org/cig/software/github/pylith/v2.2.0/pylith-2.2.0_manual.pdf
- 782 Aagaard, B. T., Knepley, M. G., and Williams, C. A. (2013). A domain decomposition approach
783 to implementing fault slip in finite-element models of quasi-static and dynamic crustal
784 deformation. *Journal of Geophysical Research Solid Earth*, 118, 3059–3079.
785 <https://doi.org/10.1002/jgrb.50217>
- 786 Araki, E., Saffer, D. M., Kopf, A. J., Wallace, L. M., Kimura, T., Machida, Y., Ide, S., Davis, E.,
787 and IODP Expedition 365 shipboard scientists (2017). Recurring and triggered slow-slip events
788 near the trench at the Nankai Trough subduction megathrust. *Science*, 356:1157–1160.

- 789 Ariyoshi, K., Iinuma, T., Nakano, M., Kimura, T., Araki, E., Machida, Y., Sueki, K., Yada, S.,
790 Nishiyama, T., Suzuki, K., Hori, T., Takahashi, N., and Kodaira, S. (2021). Characteristics of
791 Slow Slip Event in March 2020 Revealed From Borehole and DONET Observatories. *Frontiers*
792 in Earth Science, 8.
- 793 Barker, D., Wallace, L., Woods, K., Savage, M., and TAN1809 Science Party (2019). Hiku-
794 rangi Ocean Bottom Investigation of Tremor and Slow Slip (HOBITSS V). Technical report,
795 GNS Science, Lower Hutt, NZ.
- 796 Bartlow, N.M., Miyazaki, S.I., Bradley, A.M. and Segall, P., 2011. Space-time correlation of slip
797 and tremor during the 2009 Cascadia slow slip event. *Geophysical Research Letters*, 38(18).
- 798 Beavan, J., Tregoning, P., Bevis, M., Kato, T. and Meertens, C., 2002. Motion and rigidity of the
799 Pacific Plate and implications for plate boundary deformation. *Journal of Geophysical Research: Solid Earth*, 107(B10), pp.ETG-19.
- 800 Bell, R., C. Holden, W. Power, X. Wang, and G. Downes, Hikurangi margin tsunami earthquake
801 generated by slow seismic rupture over a subducted seamount, *Earth and Planet. Sci. Lett.*, 397,
802 1-9, 2014.
- 803 Bürgmann, R. and Chadwell, D. (2014). Seafloor Geodesy. *Annu. Rev. Earth Planet. Sci.*,
804 42:509–534.
- 805 Clark, K., Howarth, J., Litchfield, N., Cochran, U. A., Turnball, J., Dowling, L., Howell, A.,
806 Berryman, K., and Wolfe, F. (2019). Geological evidence for past large earthquakes and
807 tsunamis along the Hikurangi subduction margin, New Zealand. *Marine Geology*, 412:139–172.
- 808 Cochran, U., Berryman, K., Zachariasen, J., Mildenhall, D., Hayward, B., Southall, K., Hollis,
809 C., Barker, P., Wallace, L., Alloway, B., and Wilson, K. (2006). Paleoecological insights into
810 subduction zone earthquake occurrence, eastern North Island, New Zealand. *Bulletin of the
811 Geological Society of America*, 118(9–10):1051–1074.
- 812 Coffey, G.L., Savage, H.M., Polissar, P.J., Meneghini, F., Ikari, M.J., Fagereng, Å., Morgan,
813 J.K., and Wang, M., 2021, Evidence of seismic slip on a large splay fault in the Hikurangi
814 subduction zone: *Geochemistry, Geophysics, Geosystems*, v. 22, no. 8, <https://doi.org/10.1029/2021GC009638>.
- 815 Cummings, J. A. (2006). Operational multivariate ocean data assimilation. *Quarterly Journal of
816 the Royal Meteorological Society*, 131(613).
- 817 Cummings, J. A. and Smedstad, O. M. (2013). Variational data assimilation for the global ocean.
818 In *Data Assimilation for Atmospheric, Oceanic and Hydrologic Applications* (Vol. II).
- 819 Dal Zilio, L., Lapusta, N. and Avouac, J.P., 2020. Unraveling scaling properties of slow-slip
820 events. *Geophysical Research Letters*, 47(10), p.e2020GL087477.
- 821 Davis, E. E., Villinger, H., and Sun, T. (2015). Slow and delayed deformation and uplift of the
822 outermost subduction prism following ETS and seismogenic slip events beneath Nicoya
823 Peninsula, Costa Rica. *Earth and Planetary Science Letters*.

- 826 Delahaye, E. J., Townend, J., Reyners, M. E., and Rogers, G. (2009). Microseismicity but no
827 tremor accompanying slow slip in the Hikurangi subduction zone, New Zealand. *Earth and*
828 *Planetary Science Letters*, 277(1-2):21–28.
- 829 Di Toro, G., R. Han, T. Hirose, N. De Paola, S. Nielsen, K. Mizoguchi, F. Ferri, M. Cocco,
830 and T. Shimamoto (2011), Fault lubrication during earthquakes, *Nature*, **471**, 494–498,
831 doi:[10.1038/nature09838](https://doi.org/10.1038/nature09838).
- 832 Doser, D. I. and Webb, T. H. (2003). Source parameters of large historical (1917–1961)
833 earthquakes, North Island, New Zealand. *Geophysical Journal Interna- tional*, 152(3):795–832.
- 834 Downes, G., T.H. Webb, M.J. McSaveney, C. Chague-Goff, D.J. Darby, and A. Barnett (2000),
835 The March 25 and May 17 1947 Gisborne earthquakes and tsunami: Implication for tsunami
836 hazard for East Coast, North Island, New Zealand, in *Tsunami Risk Assessment Beyond 2000: Theory, Practice and Plans*, Proceedings of Joint IOC–IUGG International
837 Workshop, V.K. Gusiakov, B.W. Levin, and O.I. Yakovenko, eds, Moscow, pp. 55-67.
838
- 839 Eberhart-Philips, D. and Bannister, S. (2015). 3-D imaging of the northern Hikurangi subduction
840 zone, New Zealand: variations in subducted sediment, slab fluids and slow slip. *Geophysical*
841 *Journal International*, 201:838–855.
- 842 Eberhart-Phillips, D. and Reyners, M. (2012). Imaging the Hikurangi Plate interface region, with
843 improved local-earthquake tomography. *Geophysical Journal International*, 190(2):1221–1242.
- 844 Eberhart-Phillips, D., Reyners, M., Bannister, S., Chadwick, M., and Ellis, S. (2010).
845 Establishing a versatile 3-D seismic velocity model for New Zealand. *Seismological Research*
846 *Letters*, 81(6).
- 847 Fagereng, Å., et al., 2019, Mixed deformation styles observed on a shallow subduction thrust,
848 Hikurangi margin, New Zealand, *Geology*, doi .org /10 .1130 /G46367.1
- 849 Frank, W.B. and Brodsky, E.E., 2019. Daily measurement of slow slip from low-frequency
850 earthquakes is consistent with ordinary earthquake scaling. *Science advances*, 5(10),
851 p.eaw9386.
- 852 Fredrickson, E. K., Wilcock, W. S., Schmidt, D. A., MacCready, P., Roland, E., Kurapov, A. L.,
853 Zumberge, M. A., and Sasagawa, G. S. (2019). Optimizing Sensor Configurations for the
854 Detection of Slow-Slip Earthquakes in Seafloor Pressure Records, Using the Cascadia
855 Subduction Zone as a Case Study. *Journal of Geophysical Research: Solid Earth*.
- 856 Gagnon, K., C. D. Chadwell, and E. Norabuena Measuring the onset of locking in the Peru-Chile
857 trench with GPS and acoustic measurements, *Nature*, 434(7030), 205-208,doi:
858 10.1038/nature03412,2005.
- 859 Gomberg, J., Wech, A., Creager, K., Obara, K. and Agnew, D., 2016. Reconsidering earthquake
860 scaling. *Geophysical Research Letters*, 43(12), pp.6243-6251.
- 861
- 862

- 863 Hamling, I. J., Wright, T. J., Hreinsdóttir, S., and Wallace, L. M. (2022). A Snapshot of New
864 Zealand's Dynamic Deformation Field From Envisat InSAR and GNSS Observations Between
865 2003 and 2011. *Geophysical Research Letters*, 49(2).
- 866 Hayward, B. W., Sabaa, A. T., Grenfell, H. R., Cochran, U. A., Clark, K. J., Litchfield, N. J.,
867 Wallace, L., Marden, M., and Palmer, A. S. (2015). Foraminiferal record of Holocene paleo-
868 earthquakes on the subsiding south-western Poverty Bay coastline, New Zealand. *New Zealand
869 Journal of Geology and Geophysics*, 58(2).
- 870 Helber, R. W., Townsend, T. L., Barron, C. N., Dastugue, J. M., and Carnes, M. R. (2013).
871 Validation Test Report for the Improved Synthetic Ocean Profile (ISOP) System, Part I:
872 Synthetic Profile Methods and Algorithm. Technical report, Naval Research Lab Stennis
873 Detachment Stennis Space Center MS Oceanography Div.
- 874 Hooper, A. J. (2008). A multi-temporal InSAR method incorporating both persistent scatterer
875 and small baseline approaches. *Geophysical Research Letters*, 35(16).
- 876 Hooper, A., Bekaert, D., Spaans, K., and Arikan, M. (2012). Recent advances in SAR
877 interferometry time series analysis for measuring crustal deformation. *Tectonophysics*, 514–
878 517:1–13.
- 879 Ide, S., Beroza, G.C., Shelly, D.R. and Uchide, T., 2007. A scaling law for slow
880 earthquakes. *Nature*, 447(7140), pp.76–79.
- 881 Im, K., Saffer, D., Marone, C. and Avouac, J.P., 2020. Slip-rate-dependent friction as a universal
882 mechanism for slow slip events. *Nature Geoscience*, 13(10), pp.705–710.
- 883 Inoue, T., Ito, Y., Wallace, L. M., Yoshikawa, Y., Inazu, D., Garcia, E. S. M., Muramoto, T.,
884 Webb, S. C., Ohta, K., Suzuki, S., and Hino, R. (2021). Water depth dependence of long-range
885 correlation in nontidal variations in seafloor pressure. *Geophysical Research Letters*.
- 886 Ito, Y., Hino, R., Kido, M., Fujimoto, H., Osada, Y., Inazu, D., Ohta, Y., Iinuma, T., Ohzono,
887 M., Miura, S., Mishina, M., Suzuki, K., Tsuji, T., and Ashi, J. (2013). Episodic slow slip events
888 in the Japan subduction zone before the 2011 Tohoku-Oki earthquake. *Tectonophysics*.
- 889 Kato, A., Obara, K., Igarashi, T., Tsuruoka, H., Nakagawa, S., and Hirata, N. (2012).
890 Propagation of Slow Slip Leading Up to the 2011 M w 9.0 Tohoku-Oki Earthquake. *Science*,
891 335:705–708.
- 892 Koulali, A., McClusky, S., Wallace, L. M., Allgeyer, S., Tregoning, P., D'Anastasio, E., and
893 Benavente, R. (2017). Slow slip events and the 2016 Te Araroa M w 7.1 earthquake interaction:
894 Northern Hikurangi subduction, New Zealand. *Geophysical Research Letters*, 44:8336–8344.
- 895 Leeman, J.R., Saffer, D.M., Scuderi, M.M. and Marone, C., 2016. Laboratory observations of
896 slow earthquakes and the spectrum of tectonic fault slip modes. *Nature communications*, 7(1),
897 p.11104.

- 898 Lellouche, J.-M., Greiner, E., Bourdallé-Badie, R., Garric, G., Melet, A., Drévillon, M., Bricaud,
899 C., Hamon, M., Le Galloudec, O., Regnier, C., Candela, T., Testut, C.-E., Gasparin, F.,
900 Ruggiero, G., Benkiran, M., Drillet, Y., and Le Traon, P.-Y. (2021). The Copernicus Global
901 1/12° Oceanic and Sea Ice GLORYS12 Reanalysis. *Frontiers in Earth Science*, 9.
- 902 Lin, J. T., Aslam, K. S., Thomas, A. M., and Melgar, D. (2020). Overlapping regions of
903 coseismic and transient slow slip on the Hawaiian decollement. *Earth and Planetary Science
Letters*, 544.
- 905 Liu, Y. and Rice, J.R., 2007. Spontaneous and triggered aseismic deformation transients in a
906 subduction fault model. *Journal of Geophysical Research: Solid Earth*, 112(B9).
- 907 McCaffrey, R. (2009). Time-dependent inversion of three-component continuous GPS for steady
908 and transient sources in northern Cascadia. *Geophysical Research Letters*, 36(L07304).
- 909 Menemenlis, D., Campin, J.-M., Heimbach, P., Hill, C. N., Lee, T., Nguyen, A. T., Schodlok, M.
910 P., and Zhang, H. (2008). ECCO2: High resolution global ocean and sea ice data synthesis.
911 *Mercator Ocean Quarterly Newsletter*, 31(October).
- 912 Michel, S., Gualandi, A. and Avouac, J.P., 2019. Similar scaling laws for earthquakes and
913 Cascadia slow-slip events. *Nature*, 574(7779), pp.522-526.
- 914 Miyazaki, S.I., Segall, P., McGuire, J.J., Kato, T. and Hatanaka, Y., 2006. Spatial and temporal
915 evolution of stress and slip rate during the 2000 Tokai slow earthquake. *Journal of Geophysical
916 Research: Solid Earth*, 111(B3).
- 917 Petersen, M. D., Shumway, A. M., Powers, P. M., Mueller, C. S., Moschetti, M. P., Frankel, A.
918 D., et al. (2020). The 2018 update of the US national seismic hazard model: Overview of model
919 and implications. *Earthquake Spectra*, 36(1), 5–41. <https://doi.org/10.1177/8755293019878199>
- 920 Pizer, C., K. Clark, J. Howarth, A. Howell, J. Delano, B. W. Hayward, N. Litchfield; A 5000 yr
921 record of coastal uplift and subsidence reveals multiple source faults for past earthquakes on the
922 central Hikurangi margin, New Zealand. *GSA Bulletin* 2023;
923 doi: <https://doi.org/10.1130/B36995.1>
- 924 Polster, A., Fabian, M. and Villinger, H., 2009. Effective resolution and drift of Paroscientific
925 pressure sensors derived from long-term seafloor measurements. *Geochemistry, Geophysics,
926 Geosystems*, 10(8).
- 927 Radiguet, M., Perfettini, H., Cotte, N., Gualandi, A., Valette, B., Kostoglodov, V., Lhomme, T.,
928 Walpersdorf, A., Cabral Cano, E., and Campillo, M. (2016). Triggering of the 2014 Mw 7.3
929 Papanoa earthquake by a slow slip event in Guerrero, Mexico. *Nature Geoscience*, 9(11):829–
930 833.
- 931 Ramos, M. D. and Huang, Y. (2019). How the Transition Region Along the Cascadia Megathrust
932 Influences Coseismic Behavior: Insights From 2-D Dynamic Rupture Simulations. *Geophysical
933 Research Letters*.

- 934 Reyners, M., Eberhart-Phillips, D., and Martin, S. (2014). Prolonged canterbury earth- quake
935 sequence linked to widespread weakening of strong crust. *Nature Geoscience*, 7(1).
- 936 Romanet, P. and Ide, S. (2019). Ambient tectonic tremors in Manawatu, Cape Turnagain,
937 Marlborough, and Puysegur, New Zealand. *Earth, Planets and Space*, 71(1).
- 938 Rowe, C.D., Meneghini, F., and Moore, J.C., 2011, Textural record of the seismic cycle: Strain-
939 rate variation in an ancient subduction thrust, *in* Fagereng, Å., et al., eds., *Geology of the*
940 *Earthquake Source: A Volume in Honour of Rick Sibson: Geological Society [London] Special*
941 *Publication 359*, p. 77–95, <https://doi.org/10.1144/SP359.5>.
- 942 Ruiz, S., Metois, M., Fuenzalida, A., Ruiz, J., Leyton, F., Grandin, R., Vigny, C., Madariaga, R.,
943 and Campos, J. (2014). Intense foreshocks and a slow slip event pre- ceded the 2014 Iquique
944 Mw8.1 earthquake. *Science*, 345(6201):1165–1169.
- 945 Sakaguchi, A., Chester, F., Curewitz, D., Fabbri, O., Goldsby, D., Kimura, G., Li, C.F., Masaki,
946 Y., Screamton, E.J., Tsutsumi, A. and Ujiie, K., 2011. Seismic slip propagation to the updip end of
947 plate boundary subduction interface faults: Vitrinite reflectance geothermometry on Integrated
948 Ocean Drilling Program NanTro SEIZE cores. *Geology*, 39(4), pp.395–398.
- 949 Segall, P., Rubin, A.M., Bradley, A.M. and Rice, J.R., 2010. Dilatant strengthening as a
950 mechanism for slow slip events. *Journal of Geophysical Research: Solid Earth*, 115(B12).
- 951 Shreedharan, S., Saffer, D., L.M. Wallace, and C. Williams, 2023, Ultralow frictional healing
952 explains recurring slow slip events, *Science*, 379(6633), 712–717.
953
- 954 Tadono, T., Ishida, H., Oda, F., Naito, S., Minakawa, K., and Iwamoto, H. (2014). Precise
955 Global DEM Generation by ALOS PRISM. *ISPRS Annals of the Photogrammetry, Remote*
956 *Sensing and Spatial Information Sciences*, II-4.
- 957 Tadono, T., Nagai, H., Ishida, H., Ode, F., Naito, S., Minakawa, K., and Iwamoto, H. (2016).
958 Initial Validation of the 30 m-mesh Global Digital Surface Model Generated by ALOS PRISM.
959 *The International Archives of the Photogrammetry, Remote Sensing and Spatial Information*
960 *Sciences*, ISPRS, XLI(B4):157–162.
- 961 Takaku, J. and Tadono, T. (2017). Quality updates of 'AW3D' global DSM generated from
962 ALOS PRISM. In *International Geoscience and Remote Sensing Symposium (IGARSS)*, volume
963 July-2017.
- 964 Takaku, J., Tadono, T., and Tsutsui, K. (2014). Generation of high resolution global DSM from
965 ALOS PRISM. In *International Archives of the Photogrammetry, Remote Sensing and Spatial*
966 *Information Sciences - ISPRS Archives*, volume 40.
- 967 Takaku, J., Tadono, T., Doutsu, M., Ohgushi, F., and Kai, H. (2020). Updates of aw3d30' alos
968 global digital surface model with other open access datasets. In *International Archives of the*
969 *Photogrammetry, Remote Sensing and Spatial Information Sciences - ISPRS Archives*, volume
970 43.

- 971 Takaku, J., Tadono, T., Tsutsui, K., and Ichikawa, M. (2016). Validation of “AW3D” global
972 DSM generated from ALOS prism. *ISPRS Annals of Photogrammetry, Remote Sensing and*
973 *Spatial Information Sciences*, III-4.
- 974 Takaku, J., Tadono, T., Tsutsui, K., and Ichikawa, M. (2018). Quality improvements of ‘AW3D’
975 global DSM derived from ALOS PRISM. In *International Geoscience and Remote Sensing*
976 *Symposium (IGARSS)*, volume 2018-July.
- 977 Tsutsumi, A., Fabbri, O., Karpoff, A. M., Ujiie, K., and Tsujimoto, A. (2011). Friction velocity
978 dependence of clay-rich fault material along a megasplay fault in the Nankai subduction zone at
979 intermediate to high velocities. *Geophysical Research Letters*, 38(19).
- 980 Urlaub, M., Petersen, F., Gross, F., Bonforte, A., Puglisi, G., Guglielmino, F., Krastel, S., Lange,
981 D. and Kopp, H., 2018. Gravitational collapse of Mount Etna’s southeastern flank. *Science*
982 *Advances*, 4(10), p.eaat9700.
- 983 Vallée, M., Nocquet, J.M., Battaglia, J., Font, Y., Segovia, M., Régnier, M., Mothes, P., Jarrin,
984 P., Cisneros, D., Vaca, S. and Yepes, H., 2013. Intense interface seismicity triggered by a
985 shallow slow slip event in the Central Ecuador subduction zone. *Journal of Geophysical*
986 *Research: Solid Earth*, 118(6), pp.2965–2981.
- 987 Wallace, L. M. (2020). Slow Slip Events in New Zealand. *Annual Review of Earth and Planetary*
988 *Sciences*, 48:175–203.
- 989 Wallace, L. M. and Beavan, J. (2010). Diverse slow slip behavior at the Hikurangi subduction
990 margin, New Zealand. *Journal of Geophysical Research: Solid Earth*, 115(B12402).
- 991 Wallace, L. M. and Eberhart-Philips, D. (2013). Newly observed, deep slow slip events at the
992 central Hikurangi margin, New Zealand: Implications for downdip variability of slow slip and
993 tremor, and relationship to seismic structure. *Geophysical Research Letters*, 40:5393–5398.
- 994 Wallace, L. M., Barnes, P., Beavan, J., Van Dissen, R., Litchfield, N., Mountjoy, J., Langridge,
995 R., Lamarche, G., and Pondard, N. (2012a). The kinematics of a transition from subduction to
996 strike-slip: An example from the central New Zealand plate boundary. *Journal of Geophysical*
997 *Research: Solid Earth*, 117(B2).
- 998 Wallace, L. M., Beavan, J., Bannister, S., and Williams, C. (2012b). Simultaneous long-term and
999 short-term slow slip events at the Hikurangi subduction margin, New Zealand: Implications for
1000 processes that control slow slip event occurrence, duration, and migration. *Journal of*
1001 *Geophysical Research*, 117(B11402).
- 1002 Wallace, L. M., Beavan, J., McCaffrey, R., and Darby, D. (2004). Subduction zone coupling and
1003 tectonic block rotations in the North Island, New Zealand. *Journal of Geophysical Research:*
1004 *Solid Earth*, 109(B12).
- 1005 Wallace, L. M., Kaneko, Y., Hreinsdóttir, S., Hamling, I., Peng, Z., Bartlow, N., D’Anastasio, E.,
1006 and Fry, B. (2017). Large-scale dynamic triggering of shallow slow slip enhanced by overlying
1007 sedimentary wedge. *Nature Geoscience*, 10:765–770.

- 1008 Wallace, L. M., Webb, S. C., Ito, Y., Mochizuki, K., Hino, R., Henrys, S., Schwartz, S. Y., and
1009 Sheehan, A. F. (2016). Slow slip near the trench at the Hikurangi subduction zone, New Zealand.
1010 Science, 352(6286):701–704.
- 1011 Wallace, L.M., Saffer, D.M., Barnes, P.M., Pecher, I.A., Petronotis, K.E., LeVay, L.J., and the
1012 Expedition 372/375 Scientists, 2019. *Hikurangi Subduction Margin Coring, Logging, and*
1013 *Observatories*. Proceedings of the International Ocean Discovery Program, 372B/375: College
1014 Station, TX (International Ocean Discovery Program). [https://doi.org/10.14379/
1015 iodp.proc.372B375.2019](https://doi.org/10.14379/iodp.proc.372B375.2019)
- 1016 Werner, C., Wegmüller, U., Strozzi, T., and Wiesmann, A. (2000). GAMMA SAR and
1017 interferometric processing software. In European Space Agency, (Special Publication) ESA SP,
1018 number 461.
- 1019 Wilcock, W. S. D., Manalang, D. A., Fredrickson, E. K., Harrington, M. J., Cram, G., Tilley, J.,
1020 Burnett, J., Martin, D., Kobayashi, T., and Paros, J. M. (2021). A Thirty- Month Seafloor Test of
1021 the A-0-A Method for Calibrating Pressure Gauges. Frontiers in Earth Science, 8.
- 1022 Williams, C. A. and Wallace, L. M. (2015). Effects of material property variations on slip
1023 estimates for subduction interface slow-slip events. Geophysical Research Letters, 42:1113–
1024 1121.
- 1025 Williams, C. A. and Wallace, L. M. (2018). The Impact of Realistic Elastic Properties on
1026 Inversions of Shallow Subduction Interface Slow Slip Events Using Seafloor Geodetic Data.
1027 Geophysical Research Letters, 45:1–9.
- 1028 Williams, C. A., Eberhart-Phillips, D., Bannister, S., Barker, D. H. N., Henrys, S., Reyners, M.,
1029 and Sutherland, R. (2013). Revised Interface Geometry for the Hikurangi Subduction Zone, New
1030 Zealand. Seismological Research Letters, 84(6):1066–1073.
- 1031 Wong I, Kulkarni R, Zachariasen J, Lawrence M, Hanson K, Clague J, Ostena D, Youngs R,
1032 LaForge R, McCann M. Characterising the Cascadia Subduction Zone for Seismic Hazard
1033 Assessments. Proceedings of the 10th National Conference on Earthquake Engineering,
1034 Anchorage, AK, 2014.
- 1035 Woods, K., S. Webb, L. M. Wallace Y Ito, C Collins, N Palmer, R Hino, MK Savage, DM
1036 Saffer, EE Davis, DHN Barker, 2022, Using sealoor geodesy to detect vertical deformation at the
1037 Hikurangi subduction zone: Insights from self-calibrating pressure sensors and ocean general
1038 circulation models, J. Geophys. Res., <https://doi.org/10.1029/2022JB023989>
- 1039 Yohler, R., Bartlow, N., Wallace, L. M., and Williams, C. (2019). Time-Dependent Behav- ior of
1040 a Near-Trench Slow-Slip Event at the Hikurangi Subduction Zone. Geochemistry, Geophysics,
1041 Geosystems, 20(8).
- 1042 Yokota, Y. and Ishikawa, T. (2020). Shallow slow slip events along the Nankai Trough detected
1043 by GNSS-A. Science Advances, 6(3).